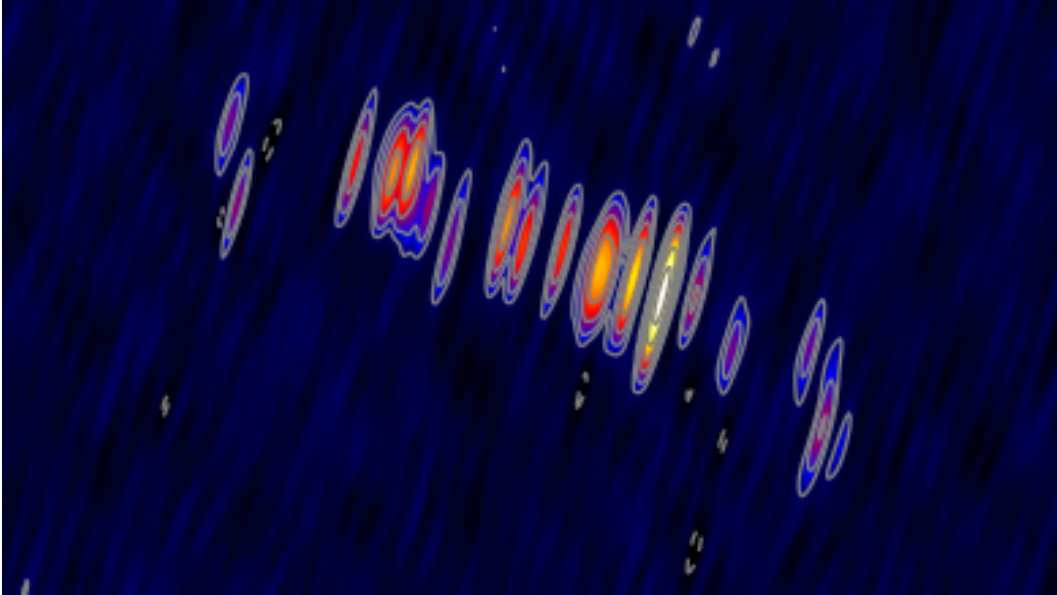


Calibration and imaging of GMVA observations of NGC1052



Bachelorarbeit

vorgelegt von Anne-Kathrin Baczko
Erlangen, 27.09.2012

Erlangen Centre for Astroparticle Physics
Dr. Remis Sternwarte Bamberg
Friedrich-Alexander-Universität
Erlangen-Nürnberg
Universität Würzburg

1. Gutachter: Prof. Dr. Jörn Wilms
2. Gutachter: Prof. Dr. Matthias Kadler



ERLANGEN CENTRE
FOR ASTROPARTICLE
PHYSICS



FRIEDRICH-ALEXANDER
UNIVERSITÄT
ERLANGEN-NÜRNBERG

Abstract

This Bachelor thesis describes the calibration process of 86.2 GHz very-long-baseline interferometry observations of NGC 1052 obtained with the Global millimeter VLBI Array (GMVA). The galaxy hosts an active galactic nucleus (AGN) and shows two radio-emitting jets with an unresolved emission gap in between. At its distance of about 20 Mpc, the archived resolution of 0.5 mas corresponds to linear scales of 0.5 pc. Therefore it is possible to analyze the innermost structure with *mm* interferometry.

AGNs emit over the complete electromagnetic spectrum, are brighter than a whole galaxy and have a Super Massive Black Hole (SMBH) in the center. The unified model for AGNs is capable of explaining the most aspects of this class, but the detailed physical conditions are not completely understood. The combination of the short distance to the object and observations at *mm*-wavelength provides the chance to study its radio jet at sub-parsec scales very close to the central engine.

The observations took place at 2004 October 9 and 10 with the telescopes Effelsberg, Pico Veleta, Plateau de Bure, Metsähovi in Europe and the VLBA antennas Hancock, Fort Davis, North Liberty, Owens Valley, Pie Town, Kitt Peak, Mauna Kea and Los Alamos in the USA.

The calibration of the data was made with the Astronomical Image Processing System (AIPS). The “*global fringe fitting*” algorithm was used to correct for the instrumental delays between the individual sub-bands, by finding the interferometric delay and delay rate (FRING). The amplitude calibration was made using the technical characteristics of the observing dishes, and the measured calibration values and weather data recorded at each station. At the high frequency used, given the short coherence times and the big influence of atmospheric changes, the calibration is a challenging task. I calibrated the data and produced an image of the source via hybrid mapping. This is the first-ever image of NGC 1052 at this high frequency (see cover).

Contents

1	Introduction	1
2	Active Galactic Nuclei	2
2.1	Eddington luminosity	3
2.2	The unified model	3
2.2.1	Jets	4
2.3	Subclasses of AGN	6
3	Radio Interferometry	8
3.1	Astronomical principles	8
3.1.1	Flux and Power	8
3.1.2	One radio antenna	9
3.2	2-element interferometer	10
3.3	Consideration of a bandpass	11
3.4	Finite Source Size	12
3.5	Multi-baseline interferometry	12
3.6	The uv -plane	12
4	Millimeter-VLBI Observations of NGC1052	14
4.1	The GMVA	14
4.2	GMVA Observation of NGC1052	15
4.2.1	The source: NGC1052	15
4.2.2	The GMVA observation	17
5	Data Reduction	19
5.1	Introduction to AIPS	19
5.1.1	The Most Important Tasks	20
5.1.2	The Most Important Vverbs	21
5.2	Walk Through The Calibration	21
5.2.1	Phase Calibration	21
5.2.2	Amplitude calibration	27
6	Imaging Results	29
	Bibliography	III
A	Erklärung	VII

1 | Introduction

The human being is characterized by its thirst for knowledge. This is one of the forces which moves the world. We want to know in which way things work and what lies behind problems of everyday life. This is the heart of science.

One of the biggest and most fascinating mysteries is seen during the night, when the sun sets down. Then the sky shows itself from its most beautiful side. In every direction little pointlike sources are pinned on the black firmament. Humans are mesmerized by it and draw pictures of their lives with the help of the stars.

Since the beginning of the 20th century, we know that every light we see, or not, can be described by an electromagnetic wave. But our eyes are only capable of recognizing a small band of the electromagnetic spectrum, the optical light. As the wavelength gets shorter it goes into the X-ray regime, if it gets longer it goes through infrared towards the radio regime. To look in these wavelength ranges we have to build other eyes which can see it.

At this point the earth protecting atmosphere turns out to be a problem. Every photon with a wavelength shorter than about 5 mm is limited by absorption, except for the little band where the optical light comes through. A better view is guaranteed if going into space, for most cases. The domain of the wavelengths longer than 5 mm is the radio astronomy. One can build big ground-based radio telescopes, which is less expensive than launching them into outer space. We can get easily big collecting surfaces with large radio dishes, such as the Effelsberg telescope with a diameter of 100m or the world's largest filled telescope Arecibo in Puerto Rico with 305m diameter, fixed in the ground. Concerning resolution, even the largest dishes are comparable to the human eye, due to the long observing wavelengths.

In the seek for higher resolution, there is a boundary in diameter over which it is not possible or very expensive and time consuming to build a telescope, especially if it should be steerable. The next step in the quest for resolution is to build a radio interferometer. This concept is based on the physical properties of electromagnetic waves of adding up the fields. From optics we know the Michelson interferometer. There it is used that two beams which have the same wavelength can be added constructive or destructive depending on the phase. The maximum resolution can be obtained with a technique called "Very Long Baseline Interferometry" (VLBI). Which combines radio telescopes across the world, synthesizing a telescope as large as the whole Earth and yielding resolutions far below the arc second. In my thesis I make use of this technique to look at the very inner structure of the elliptical galaxy NGC1052, close by its super massive black hole (SMBH). The concepts of radio interferometry and the challenging steps in analysing the data are discussed.

2 | Active Galactic Nuclei

An extremely interesting class of galaxies is those of the objects containing a so called “active nucleus”. These nuclei are brighter than a whole galaxy. They have very large structures over the whole electromagnetic spectrum. In contrast to “normal galaxies” their activity can not be described by stellar emission. A look at Fig. 2.1 and Fig. 2.2 helps to understand how big is the amount of released energy. The bright spot at the upper left of the images is a foreground star and the other spot is not a star, but the core of a whole galaxy.

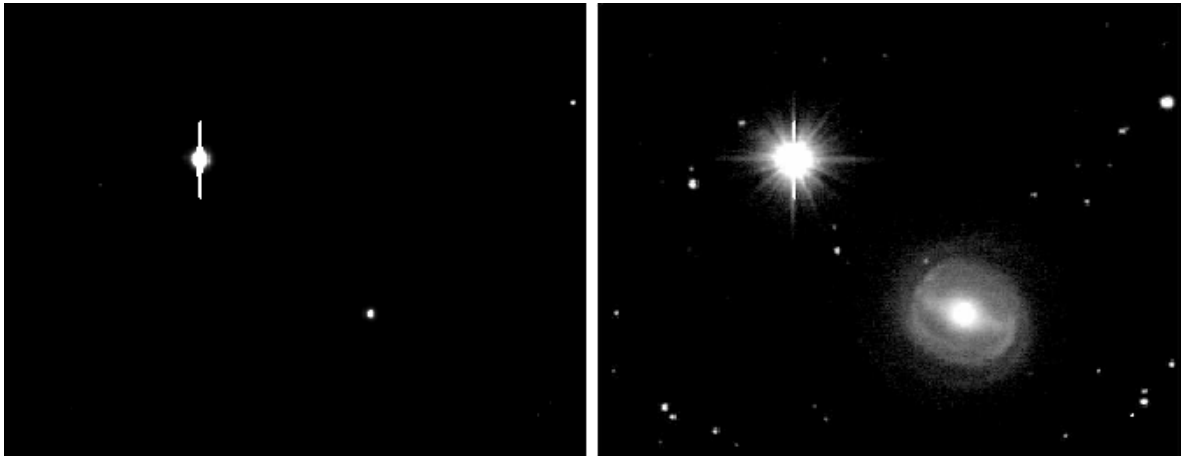


Figure 2.1: optical image of NGC3783 with linear intensity scale. The left source is a foreground star. (Wilms & Kadler, 2010)

Figure 2.2: logarithmic intensity scale of NGC3783. The right star like point in the linear scale image corresponds to a galaxy! (Wilms & Kadler, 2010)

Because of the extreme brightness Active Galactic Nuclei (AGN) are seen up to very large distances. The most distant and most luminous kind of AGN are Quasars ¹. A good fraction of them has even been detected at redshifts larger than 4. To understand the meaning of this, let us look at the formula for the cosmological redshift. It gives the size of the universe $a(t_{\text{em}})$ when the light was emitted in comparison to today's:

$$a(t_{\text{em}}) = \frac{1}{1+z} \tag{2.0.1}$$

For example, for the source SDSS 023137.65–072854.4, cataloged by the Sloan Digital Sky Survey with a redshift of $z = 5.4135$, the size of the universe was $0.1559 \times a(\text{today})$. (Carroll & Ostlie (2007)).

This redshift is caused by the accelerating expansion of the universe and such a large z denotes a velocity of the source near the velocity of light. To see such a distant source it has to be very bright. There arises the question where such a big amount of energy comes from (see next section). Later in this chapter we will have a look at the actual best AGN model.

¹QUAsi StellAr Radio Source

Furthermore, if the size of the universe changes with time and so the scale factor $a(t)$, the density changes by $a(t)^3$. This means that the space was much denser the time the light from the quasar was emitted and therefore the quasars were much closer to each other, than the galaxies today. These sources give us the chance to look back in time at the early universe. For further details on cosmology see e.g. Mukhanov (2005) Quasars are just a subgroup of AGNs, at which we will have a closer look later.

2.1 Eddington luminosity

The output of physical processes is determined by the ratios of the existing forces. Eddington introduced the maximum luminosity (Eddington Limit L_{ED}) that is allowed for a star, or other heavy object, if it remains in hydrostatic equilibrium. The main forces are due to gravitation and due to radiation pressure.

$$L_{\text{ED}} = \frac{4\pi M c m_p}{\sigma_T} = 1.3 \times 10^{38} \text{ erg s}^{-1} \frac{M}{M_{\odot}} \quad (2.1.1)$$

with the Thomson cross section σ_T , the Mass M of the gravitating object, the proton mass m_p and the velocity of light c . In the evolution of stars the effect of luminosity variability shows that the stars are not always in equilibrium. For example for a luminosity higher than L_{ED} the radiation pressure exceeds the gravitational one and mass loss occur.

The same formula is true for accreting objects, like black holes. Here we obtaine the maximum possible energy release from the conversion of potential to kinetic energy.

2.2 The unified model

Before looking at the different kinds of AGN I will introduce the so called ‘‘unified model’’ (Antonucci & Miller (1985); Lawrence (1987); Antonucci (1993); Urry & Padovani (1995)). It is ‘unified’ because it is capable of describing all the different aspects of AGN into one picture.

An AGN consists in principle of six parts: the Super Massive Black Hole (SMBH, $M \sim 10^8 M_{\odot}$) in the center, an accretion disc ($r \sim 10^{-3} \text{ pc}^2$), a torus around it ($r \sim 1 - 10 \text{ pc}$), the broad line region (BLR, $r \sim 0.01 - 0.1 \text{ pc}$) in the near of the SMBH, the narrow line region (NLR, $r \sim 100 - 1000 \text{ pc}$) farther away and for some cases jets. Fig. 2.3 illustrates this picture. Let us have a detailed look at the individual parts. It is almost clear that there are massive black holes in the center of all galaxies. In the case of AGN accretion onto a very massive object (e.g., the SMBH) is the the only known astrophysical process to release such a big amount of energy. During the accretion of the material onto the black hole the released potential energy causes a heating of the accretion disc. The in this way emitted optical brightness is known as the ‘‘big blue bump’’.

Near to the accretion disc is the BLR. The number density of electrons is very height, up to $10^{16} \text{ e}^{-} \text{ m}^{-3}$ (see Carroll & Ostlie (2007)). Therefore, frequently collisions make forbidden transitions impossible, for which the particles need to be in a long-lived metastable state. The name of the BLR comes from the broad spectral lines, which arise from the height velocities.

The cold dust torus is located at some parsecs of distance from the central engine. If one is looking straight onto it, the only emission from the regions behind comes from Compton scattering.

The NLR is located farther away from the central region. Here the number density of electrons is much lower than in the BLR³, so there also appear forbidden lines. The velocity of the particles is lower than in the BLR, therefore the spectral lines are narrower.

The last component of the unified model is the jet, that evolves perpendicularly to the accretion disc. Though it is not a characteristic of every AGN. The AGN is called radio loud if there is a radio emitting jet, if not it is radio quiet.

²One parsec is the distance from which the radius of the Earth’s orbit, 1 AU, cover an angle of 1’’

³only about 10^{10} m^{-3} Carroll & Ostlie (2007)

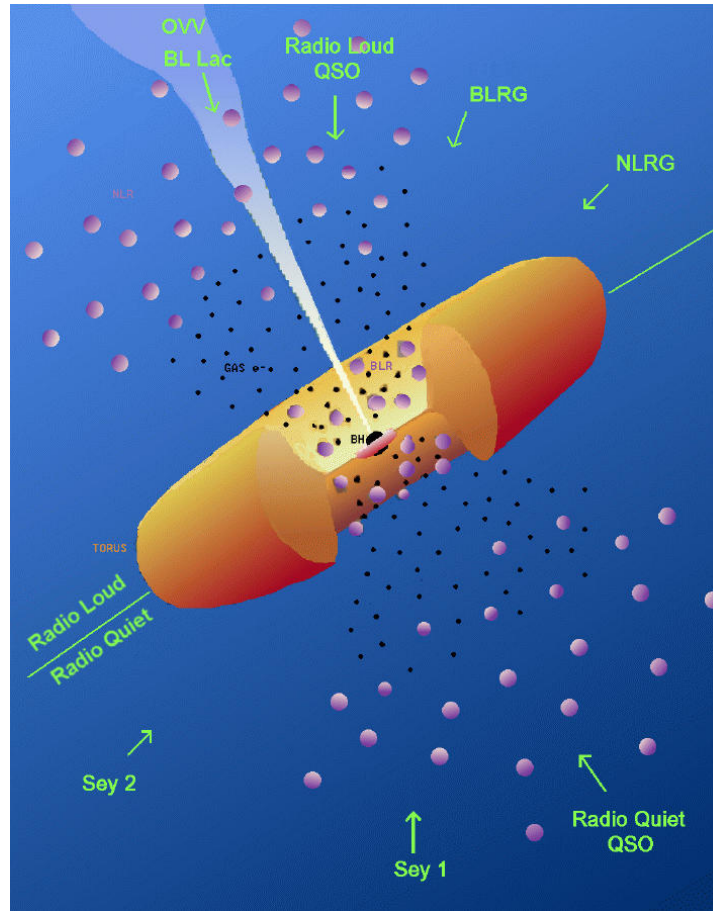


Figure 2.3: *The AGN unified model; (Urry & Padovani (1995))*

2.2.1 Jets

Jets consists of collimated plasma outflows, that are not continuous but have structure. Even at big redshifts it is possible to imagine these different components (or “blobs”).

The production of extragalactic jets is not fully understood, but it is connected to the accreting SMBH

There are some things that were observed. Especially the spectral energy distribution (SED) of AGNs indicates some physical phenomena that take place. Its emission goes typically over a big range of frequencies, from radio up to the γ -ray regime.

The combination of different scattering mechanism in the accretion disc, like Compton scattering, results for the x-ray regime in principle in a power law continuum. Because of scattering back to the accretion disk there occur the Compton Reflection Hump and Photoabsorption results in Fe $K\alpha$ and $K\beta$ peaks.

If looking closer at the radio regime, there appear strong, polarized power law spectra. This is a hint for synchrotron radiation, that is the relativistic counterpart to cyclotron radiation and results in the observed spectrum. Because of its existence there have to be magnetic fields and relativistic charged particles. For lower frequencies the medium is optical thick and a turnover appears at the point were self absorption takes place.

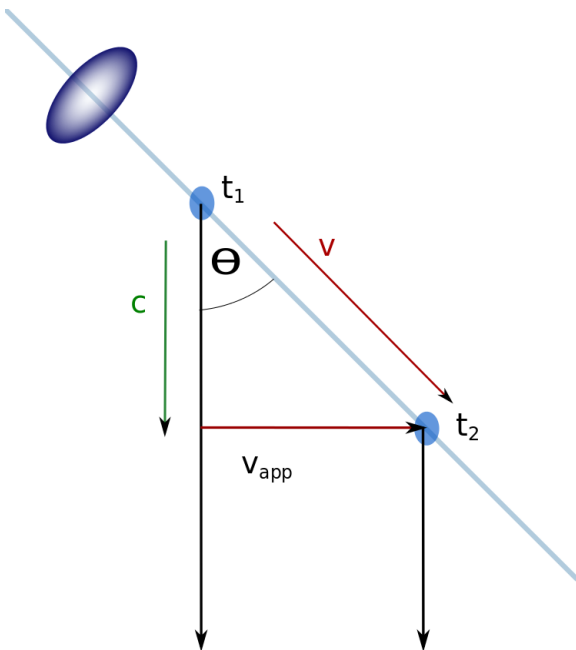
We have not looked at the production of jets yet. What is seen is a strongly collimated outflow that consists of single “blobs”. Effects like superluminal motion or one-sidedness indicate that the particles are moving at relativistic speeds. It is most likely to describe the phenomena through the assumptions of moving fluids. The physical principle that holds in the neighbourhood of such a massive object like a SMBH is the general relativity. So what can more or less describe the formation of jets is Relativistic

Hydrodynamic, that connects general relativity with the physics of fluids and shock waves. Numerical simulations including this theory and the processes of radiation transports can, in the most general cases, describe the observations (see Perucho (2008) and Rybicki & Lightman (2004)). But there is much that is not understood until today and we need more observations and physical properties to describe what is seen.

If only one jet is observed the reason lies in the AGN's orientation relative to the observer. This effect is called the "relativistic boosting", that causes parts of the jet (one of the two) to be invisible. Normally the jet which is less bright is called counterjet.

The "superluminal motion" is a second effect that may appear. We talk of superluminal motion when the speed of selected regions in the jet seems to be faster than the light. As the angle between jet orientation and line of sight gets smaller, the apparent velocity gets higher. The same effect occurs when the original jet speed gets higher.

In Fig. 2.4 it is seen how a blob is traveling along the line of sight with the velocity v . The two black arrows are pointing in the direction to the observer.



The velocity of the blob is \mathbf{v} and points under the angle Θ to the line of sight. The blob needs the time $\Delta t_{\text{em}} = t_2 - t_1$ while traveling the shown distance along the jet. The information of the location of the blob travels with the speed of light c . The time between the registration of the blobs is:

$$\Delta t = \Delta t_{\text{em}}(1 - \beta \cos(\Theta)). \quad (2.2.1)$$

Where $\beta = \frac{v}{c}$. The traveled distance on the sky between the two observations:

$$\Delta s = \sin(\Theta) v \Delta t_{\text{em}}. \quad (2.2.2)$$

In the end one gets through these simple geometric considerations the apparent velocity of the blob:

$$v_{\text{app}} = \frac{\Delta s}{\Delta t} = \frac{v \sin(\Theta)}{1 - \beta \cos(\Theta)} \quad (2.2.3)$$

For further details on the equations see Rees (1966)

Figure 2.4: Superluminal motions: the jet outflows seems to be faster than the light. This sketch describes a "blob" traveling at speed v close to c , that emits light in instants t_1 and t_2 . See text for details

The already introduced "relativistic boosting" entails a dimming of one jet.

If a particle travels at relativistic speeds and emits radiation one have to consider the Doppler effect. To obtain the observed frequency, the common way is to Lorentz transform the wave factor \mathbf{k} . The transformation of the first component is:

$$k_{\text{em}}^{(0)} = \gamma \left(k_{\text{obs}}^{(0)} - \frac{v}{c} k_{\text{obs}}^{(1)} \right), \quad (2.2.4)$$

where $\gamma = (1 - \beta^2)^{-1/2}$.

including $k^{(0)} = \omega/c$, $k_{\text{obs}}^{(1)} = \cos(\Theta)\omega_{\text{obs}}/c$ and $\omega = 2\pi\nu$ the final equations is:

$$\nu_{\text{obs}} = \nu_{\text{em}} \frac{\sqrt{1 - \beta^2}}{(1 - \beta \cos(\Theta))}. \quad (2.2.5)$$

This defines the relativistic Doppler factor, that compares the emitted and the observed frequency

$$D = \frac{\nu_{\text{obs}}}{\nu_{\text{em}}} = \frac{1}{\gamma(1 - \beta \cos(\Theta))}. \quad (2.2.6)$$

To get a connection to the flux density S_ν one can proof that S_ν/ν^3 is invariant under Lorentz transformations (e.g. Rybicki & Lightman (2004)). So, from $S_{\nu_{\text{obs}}}/\nu_{\text{obs}}^3 = S_{\nu_{\text{em}}}/\nu_{\text{em}}^3$ and knowing that the observed intensity spectrum is described by a power law ($S \sim \nu^\alpha$) (Lind & Blandford (1985)) one obtains

$$S(\nu_{\text{obs}}) = D^{3-\alpha} S(\nu_{\text{em}}). \quad (2.2.7)$$

Comparing the flux densities of an approaching and a receding jet component (Eq. 2.2.8) the presence of one-sided jets is explained.

$$\frac{S_{\text{approaching}}}{S_{\text{receding}}} = \left(\frac{1 + \beta \cos(\Theta)}{1 - \beta \cos(\Theta)} \right) \quad (2.2.8)$$

A often used term is the “core” of the jet. It is the base where the jet begins to be visible and should not be confused with the central engine (SMBH). At distances shorter to the SMBH the jet is invisible, due to synchrotron self-absorption. If the optical depth τ is about 1 the jet becomes visible and that part is known as the “core”, it is the brightest part of the jet. If two jets are seen, there should be two cores. At the end of the jet, some kilo parsec away, it can end in “radio lobes”. Those are thought to be the area, where the particles of the jet are interacting with the intergalactic medium. For more information about the jet propagation and spectral energy distribution see Lobanov (1998)

2.3 Subclasses of AGN

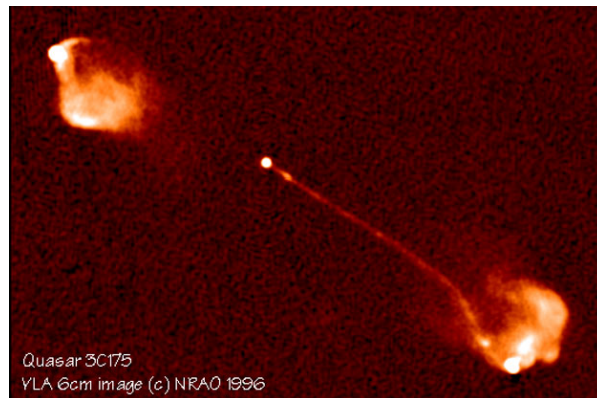


Figure 2.5: Radio image of the quasar 3C175, a FR2

Following the unification model, we know that depending on the line of sight different physical properties are observed. Before the unified model was developed, subclasses of AGN were defined. Here we provide an overview of the historical classification. (In Carroll & Ostlie (2007) this is discussed in more detail)

Quasars (**QU**Asi **Stell**Ar **R**adio **S**ource) are the most luminous kind of AGN. They are called “quasars” if strong in the radio regime and **QSO** (**Q**uasi **S**tellar **O**bject) if strong in the optical. They are the most distant ones and appear star like (therefore “quasi stellar objects”). But with the technique of radio interferometry (will be explained in the next chapter) it is possible to dissolve the jet structure. The bolometric brightness is very high (up to -21.5 mag Wilms & Kadler, 2010). Quasars are similar to Seyfert galaxies, but brighter. Therefore the host galaxy is not detectable at long distances.

Seyfert galaxies are less luminous and radio quiet. Most of the times the host galaxy is a spiral and can be detected. If there are only narrow forbidden line seen, it is a Seyfert of type 2. If there are also broad lines it is a Seyfert 1.

Liners (**L**ow-**I**onization **N**uclear **E**mission-line **R**egion galaxies) have a similar spectrum to Seyfert 2, but the low-ionization lines are the strongest ones.

Blazars have a jet directed toward the line of sight and so the beam effects are very high. A subclass of Blazars are BL Lac objects. It has a highly variable continuum emission, is compact and unresolved. The emission and absorption lines are weak and the spectrum is polarized, due to synchrotron emission. Another subclass of Blazars are core dominated quasars. They have prominent emission lines and a rapid variability in optical regime.

Radio galaxies are galaxies with strong emission at radio frequencies. Only about a 10 to 15% of AGN are radio emitters. Many of them are in the local universe at low redshifts.

Fanaroff & Riley developed a classification characterized by the jet appearance. So FR1 have two jets with broad ends (no hotspots) and a bright “core”. whereas FR2 have only one jet but hotspots and gets brighter toward the outer part (see Fanaroff & Riley (1974)).

3 | Radio Interferometry

The goal of this section is to describe succinctly how Very Long Baseline Interferometry (VLBI) works. But first I will introduce some astrophysical quantities and describe how the signals of an observed source can be detected by one radio telescope and how one can construct an image out of this. In the last and most complex part of this section we will discuss the VLBI in terms of a simple two-element interferometer.

3.1 Astronomical principles

The first radiowaves from outer space were discovered in the early 1930s by Karl Jansky. He was searching for radio-wavelength sources of static for Bell Laboratories, who wanted to transmit radio waves (of some meters in wavelength) over the Atlantic for telephone service.¹ The strongest source he found is in the direction of the center of the Milky Way.

This discovery set the stage for observations in the radio regime and inspired others (such as Grote Reber) to build and improve antennas to receive these waves. Reber (1988) These (antennas) are normal dipoles embedded in horns to enhance their sensitivity, but for more sensitivity it is useful to built parabolic dishes, which reflect the energy of the source to the receiving dipol. In principle a radio telescope is built like a satellite dish, tuned at another frequency and needing a much higher sensitivity to detect the weaker signals from celestial bodies.

One wants to receive as much energy from a source as possible, so it is obviously to build big telescopes with a great collecting area. The following sub-sections are based on Burke & Graham-Smith (2009), Thompson et al. (2001) and Wilms & Kadler (2010) and we are using mks-units.

3.1.1 Flux and Power

To compare different sources and telescopes it is useful to define some quantities. First of all there is the flux which is the rate at which energy E crosses the area A :

$$S \equiv \frac{\partial_t E}{A}. \tag{3.1.1}$$

But we can't measure the whole energy range of a source with one telescope. So one defines the (specific) flux density (per frequency band):

$$S_\nu = \frac{dS}{d\nu}. \tag{3.1.2}$$

The unit of measurement is the Jansky, named after the radio astronomy pioneer who first detected an extraterrestrial radio signal: $1 \text{ Jy} = 10^{-26} \text{ W m}^{-2} \text{ Hz}^{-1}$.

To obtain the whole received power we just have to integrate over the receiving area of the telescope, which gives an effektive area A_{eff} , and the used frequency band $d\nu$:

$$P = A_{\text{eff}} \cdot S = A_{\text{eff}} \int S_\nu d\nu. \tag{3.1.3}$$

¹www.nrao.edu/whatisra/hist_jansky.shtml

If the source can be resolved and has so a spatial extent, it is better to use the intensity or brightness distribution.

$$B_\nu(\theta, \phi) = \frac{dS_\nu}{d\Omega}. \quad (3.1.4)$$

Including this in the above Eq. 3.1.3 we obtain:

$$P = A_{\text{eff}} \iiint B_\nu d\nu d\Omega. \quad (3.1.5)$$

3.1.2 One radio antenna

The signal is collected and reflected by the parabolic antenna to the receiver. Only the signal of interest (at the observing frequency) is filtered and passed to the following electronics.

Up to now we called the receiving area A_{eff} . But there is a difference to the collecting area of the dish. The typical antenna pattern for a radio telescope is shown in the polar plot in Fig. 3.1 (right). It is the same for the emitting and the receiving mode. The lobes give the sensitivity in this direction. It would be better if the main lobe were thinner and there were no side lobes. Then the sensitivity to the required direction would be greater and there would be less side effects.

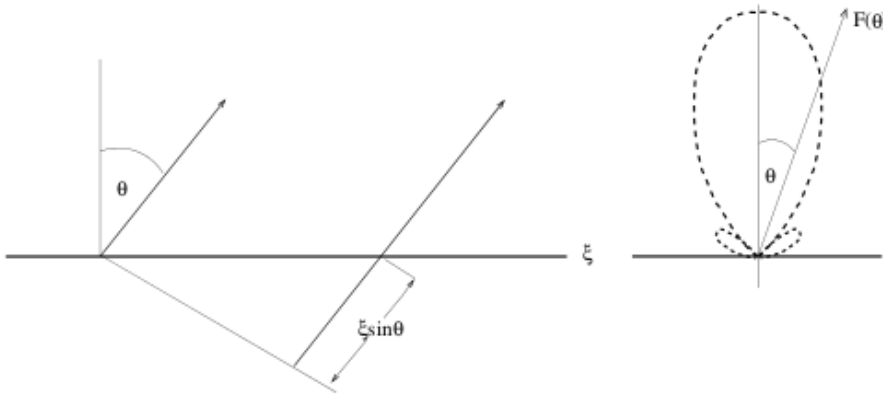


Figure 3.1: The radiation pattern of an antenna is seen for a 1D line distribution along axis ξ .(Burke & Graham-Smith (2009)

)

If the telescope is in the emitting mode, you need the correct excitation current to generate the desired radiation pattern. It is the same in the other direction. The radiation pattern is the Fourier transform of the excitation current $I(\xi)$. So one obtains:

$$F(\theta) = \int d\xi I(\xi) e^{-2\pi i \nu t}. \quad (3.1.6)$$

We know that $t = \frac{x}{c}$ and $\nu = \frac{c}{\lambda}$, therefore it follows that $t = \frac{\xi \sin \theta}{\nu \lambda}$. Applying a small angle approximation $\sin \theta = \theta$ Eq. 3.1.6 transforms into:

$$F(\theta) = \int d\xi I(\xi) e^{-i2\pi \frac{\xi \theta}{\lambda}}. \quad (3.1.7)$$

As mentioned earlier the angular resolution of a telescope depends on the diameter of the telescope and on the observed wavelength. The larger the telescope or the smaller the observing wavelength the better the angular resolution:

$$\alpha = 1.22 \times \frac{\lambda}{D}, \quad (3.1.8)$$

where α is the smallest resolvable angular distance, λ is the wavelength and D the diameter of the telescope. There is a limit in diameter where it is not possible to build a steerable radio telescope. Fortunately there is another way in getting a large D in the last equation: interferometry. In this way there is effectively a telescope with the diameter of the separation of the two single telescopes.

3.2 2-element interferometer

A schematic two element interferometer is shown Fig. 3.2. Because of the distance b_λ the same signal arrives at different times to the different elements of the interferometer. To get the information you want you need to cross-correlate the two signals, assumed they are coherent. To do this we have to insert an instrumental time delay.

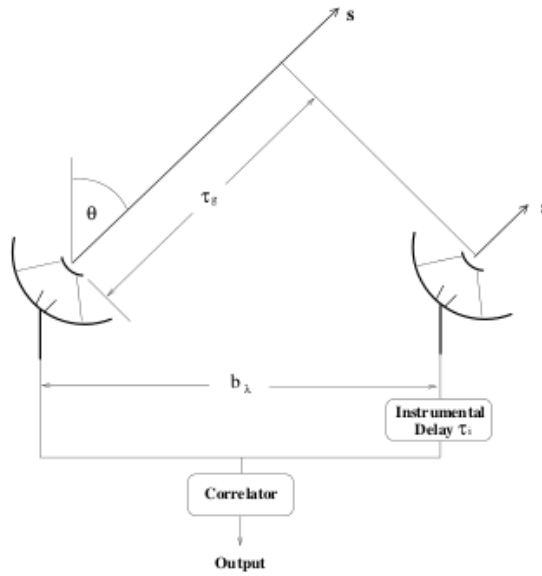


Figure 3.2: The signals at the two telescopes separated by b_λ arriving at different times. Before correlating these, an instrumental time delay can be inserted at one antenna. Burke & Graham-Smith (2009)

At one antenna the signal is:

$$x(t) = V \cos(2\pi\nu t) \quad (3.2.1)$$

The signal on the other antenna is the same plus a geometric time delay $\tau_g = \mathbf{b} \cdot \mathbf{s}/c$. Where \mathbf{s} is the vector in direction to the source and \mathbf{b} the baseline, that is the distance between two telescopes. The output signal of the correlator is called the “cross-power product” (because the solution has the dimensions of power).

From a mathematical point of view a correlation of two signals is a complex convolution. It shows how similar two signals are depending on the time lag between them.

$$r_{fg}(\tau) = \int_{-\infty}^{+\infty} dt f(t)g^*(t - \tau) = f(t) \otimes g^*(t). \quad (3.2.2)$$

The cross-power product is calculated as follows:

$$R_{xy} = \lim_{T \rightarrow \infty} \frac{1}{2T} V^2 \int_{-T}^T dt \cos(2\pi\nu t) \cos(2\pi\nu(t - \tau_g))$$

$$R_{xy} = \frac{1}{2} V^2 \cos(2\pi\nu\tau_g).$$

$2T$ is the time over that the signals are correlated during a real observation.

With $\frac{1}{2}V^2 = P = A_{\text{eff}} \cdot S$ one obtains

$$R_{xy}(\tau_g) = A_{\text{eff}} S \cos(2\pi\nu\tau_g). \quad (3.2.3)$$

So the output signal is the power sinusoidal modulated by the geometrical time delay. The cross-power product can be expressed in terms of wavelength. In this case the baseline becomes $\mathbf{b}_\lambda = \frac{\mathbf{b}}{\lambda}$ and one can express the delay as:

$$\tau_g = \frac{\mathbf{b} \cdot \mathbf{s}}{c}. \quad (3.2.4)$$

Inserting this into Eq. 3.2.3 gives:

$$R_{xy}(\tau_g) = A_{\text{eff}} S \cos(2\pi\mathbf{b}_\lambda \cdot \mathbf{s}). \quad (3.2.5)$$

The kind of interferometry used in radio astronomy is the same as in optics. The Wiener-Khinchin Theorem says that the spectral power density of a signal is the Fourier transform of its autocorrelation function (or the cross-power product):

$$S_{xy}(\nu, s) = \mathcal{F}(R_{xy}(\tau_g)) \quad (3.2.6)$$

and therefore

$$S_{xy}(\nu) = \int_{-\infty}^{+\infty} d\tau R_{xy}(\tau) e^{-i2\pi\nu\tau} = A_{\text{eff}}(\mathbf{s}) \cdot S e^{2\pi i\nu\tau_g} = A_{\text{eff}}(\mathbf{s}) \cdot S e^{2\pi i\mathbf{b}_\lambda \cdot \mathbf{s}} \quad (3.2.7)$$

Now we have the spectral power density of the observed source, as obtained with the help of a 2-element interferometer, that is the power of the source for one frequency. But that is not what we see. First of all, the whole flux of the source is re-directed by the parabolic reflector to the receiver and not only one wavelength. The receiver is responsible for selecting the frequency, that is done via a bandpass.

3.3 Consideration of a bandpass

By now only the simplest case was calculated. But under real observational circumstances, each telescope has a limited reception bandpass \mathcal{B} . This has an influence on the received signal and on the cross-correlation, because of the integration.

Assuming a rectangular bandpass:

$$G(\nu) = \prod \left(\frac{\nu - \nu_0}{\mathcal{B}} \right) = \begin{cases} 1 & ; \nu - \nu_0 \in \mathcal{B} \\ 0 & ; \text{else} \end{cases} \quad (3.3.1)$$

The whole cross-power product is:

$$P_{xy}(\tau_g) = \int_{-\infty}^{+\infty} d\nu S_{xy} G(\nu) = \int_{-\nu_0 - \frac{\mathcal{B}}{2}}^{+\nu_0 - \frac{\mathcal{B}}{2}} d\nu A_{\text{eff}}(\nu, \mathbf{s}) S(\nu) e^{2\pi i\nu\tau_g}. \quad (3.3.2)$$

After integration one obtains:

$$P_{xy}(\tau_g) = A_{\text{eff}}(\nu_0, \mathbf{s}) S(\nu_0) e^{2\pi i\nu_0\tau_g} \mathcal{B} \text{sinc}(\pi \mathcal{B} \tau_g). \quad (3.3.3)$$

The manipulation of the signal through the receiving apparatus was taken into account. Now let us have a closer look at the source itself.

3.4 Finite Source Size

Usually, any observed radio source is not point-like but has an extended structure. So we have to look at the brightness distribution $B_{\nu_0}(\mathbf{s}_0 + \sigma)$ (Eq. 3.1.5). For an extended source one has to integrate the whole cross-power product over the solid angle $d\Omega$.

The center of the source is in direction \mathbf{s}_0 and its angular extent is σ , so the vector $\mathbf{s}_0 + \sigma$ points to every point of the source.

By inserting Eq. 3.1.5 into Eq. 3.2.7 one obtains

$$S_{xy}(\nu_0, \mathbf{s}_0 + \sigma) = \iint A_{\text{eff}}(\mathbf{s}_0 + \sigma) B_{\nu_0}(\mathbf{s}_0 + \sigma) e^{2\pi i \nu (\tau_g - \tau_i)} d\Omega \quad (3.4.1)$$

Now we apply two simplifications:

- normalization of A_{eff} with respect to \mathbf{s}_0
- center frequency ν

Finally the total spectral power density is

$$S_{xy}(\mathbf{s}_0) = \int_{4\pi} A(\sigma) B_{\nu}(\sigma) e^{2\pi i (\mathbf{b}_{\lambda} \cdot (\mathbf{s}_0 + \sigma) - \nu \tau_i)} d\Omega. \quad (3.4.2)$$

3.5 Multi-baseline interferometry

The equations of the last section are valid as long as we are only correlating two telescopes. But the more telescopes the better for a radio interferometric observation, since n telescopes results in $\frac{n(n-1)}{2}$ baselines, that is the number of 2-element interferometers. So we need another quantity that describes the correlator output determined by all the possible baselines. The baseline is the distance between to telescopes. This quantity is the “*Visibility function*”:

$$V_{ij} = \int A(\sigma) B_{\nu}(\sigma) e^{2\pi i \mathbf{b}_{ij} \cdot \sigma} d\Omega \quad (3.5.1)$$

Here we assumed that $\mathbf{b}_{ij} \cdot \mathbf{s}_0 = \nu \tau_i$. The combination of the indices i and j is used to define each of the baselines.

The Visibility Function V_{ij} is the Fourier transform of the brightness distribution $B_{\nu}(\sigma)$. It is the total spectral power density with an inserted time delay canceling the geometrical delay. We want that all antennas track the source. So we define the center of the source in direction \mathbf{s}_0 as tracking center. This is the reference direction from which we obtain the geometrical delay.

Notice that the sources of interest are extended and not always very bright. They also differ in brightness with time. Under these circumstances the whole formula becomes complex and that is a problem when correcting for effects such as geometric and unintentional instrumental time delays. Because of that it is common to simultaneously measure a strong point-like calibration source. There you don't have to take into account an extended source and in the resulting visibility function you should obtain a nice sinc function with a strong central peak.

3.6 The uv -plane

The angular resolution is determined by the projected baseline normal to the source. It is convenient to define the (uv) -plane orthogonal to the direction to the phase tracking center (phase reference position). The third component w is measured in direction to \mathbf{s}_0 . This leads to the following version of the visibility:

$$V_{ij}(u, v, w) = \int_{-\infty}^{+\infty} \int_{-\infty}^{+\infty} A(l, m) B_{\nu}(l, m) e^{2\pi i [ul + vm + w(\sqrt{1-l^2-m^2}-q)]} \frac{dl dm}{\sqrt{1-l^2-m^2}}. \quad (3.6.1)$$

Assuming a small source size (l and m are small compared to the distance to the (l, m) system), Eq. 3.6.1 and therefore also w can be neglected:

$$V_{ij}(u, v) = \int_{-\infty}^{+\infty} \int_{-\infty}^{+\infty} A(l, m) B_\nu(l, m) e^{2\pi i(ul+vm)} dl dm. \quad (3.6.2)$$

The term $\sqrt{1-l^2-m^2}$ in the denominator is included in $A(l, m)$. In this form the equation is an exact two-dimensional Fourier transform. So one can get the term $A(l, m)B_\nu(l, m)$ and thus the brightness distribution by measuring the Visibility function for as many points in the (u, v) -plain as possible.

Each baseline $\mathbf{b}_{ij\lambda}$ is projected onto the uv -plane. The first options to obtain a big uv -coverage is to track the center of the source. As the earth rotates, the baseline describes an ellipse in the uv -plane. The second option is varying the positions of the antenna. For example this is made with the Very Large Array (VLA) in Socorro, New Mexico. It is an Y-shaped array of of 27 radio antennas, which can be moved on rails.



Figure 3.3: *The Very Large Array*

The next big step to increase the angular resolution is to observe with longer baselines. This is for example done with the Very Long Baseline Array (VLBA) in America. There are also other great projects all around the world, like MERLIN that is situated in Great Britain and has baselines up to 217km, that is not “very long” compared to the other mentioned Arrays but worth mentioning, or the VERA experiment in Japan that has the main goal of obtaining a 3D map of the Milky Way.

4 | Millimeter-VLBI Observations of NGC1052

The biggest VLBI array is one that covers the whole earth. A big step in that direction is the Global VLBI Array, which was used for the data calibrated in this thesis.

4.1 The GMVA

The Global mm-VLBI Array includes telescopes like the VLBA in America as well as European telescopes like Effelsberg in Germany and Pico Veleta in Spain. It is a subclass of telescopes of the global VLBI Array that are capable of operating at millimeter wavelengths. The whole global VLBI Array has also telescopes in China as well as South Africa (Hartebeesthoek Radio Astronomy Observatory) and some other European countries. An overview is seen in Fig. 4.1

The Very Long Baseline Array (VLBA) consists of 10 radio telescopes, going from Hawaii across North America up to the Virgin Islands.

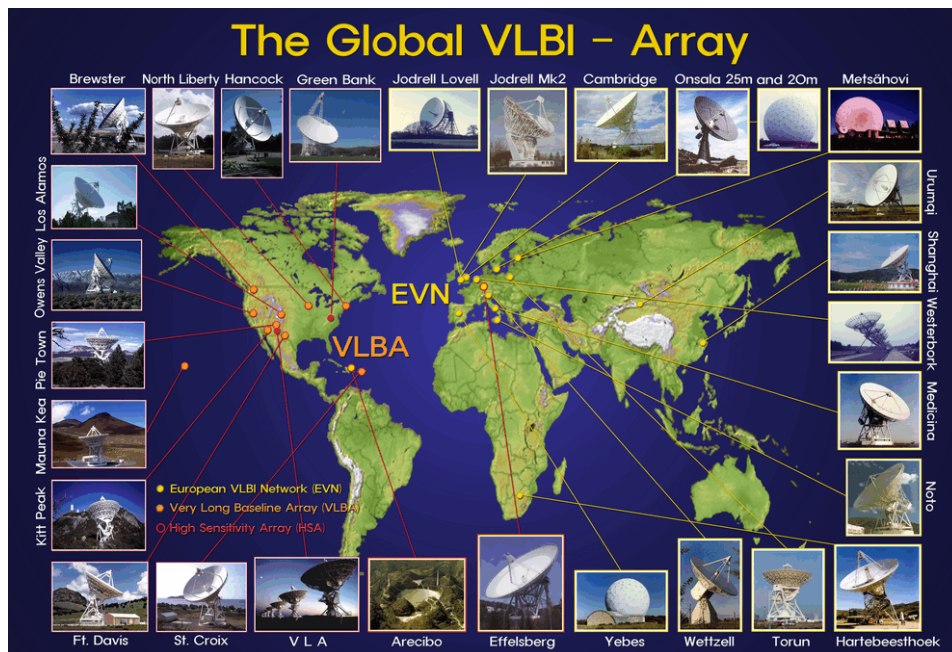


Figure 4.1: The Global VLBI Array; image credit: Tae-Hyun, Jung (MPIfR, 2004)

It is a great opportunity to be able to observe with such a large Array with so long baselines, and therefore to get the best resolution. Additional to that an operational frequency of 86.2GHz is possible

for continuum measurements. This opens the chance to observe sources with a very small angular resolutions, to study the innermost parts of AGNs.

4.2 GMVA Observation of NGC1052

4.2.1 The source: NGC1052

The elliptical galaxy NGC1052 has a very strong emission spectrum Mayall (1939). At mm-wavelengths the time varying is about one month and the amplitude varying about 0.5 – 2.5Jy (Heeschen & Puschell (1983)). Because of its direct neighborhood to us it is an excellent candidate for studying in mm-wavelength. It has a two jet structure, but even at 43 GHz, the center of the jet bases is not resolved ((Kadler, 2002)).

Redshift:	0.00537 ^(a)
Distance:	19 Mpc ^(b)
Linear scale:	0.09pc mas ⁻¹ ^(b)
L_{radio}	$\sim 4.4 \times 10^{40} \text{erg s}^{-1}$ ^(c)
Spectroscopic type:	LINER 1.9 ^(d)

Table 4.1: *selected properties of NGC1052; ^(a): Denicoló et al. (2005); ^(b): with $H_0 = 71 \text{ km s}^{-1} \text{ pc}^{-1}$; ^(c): Wrobel (1984); ^(d): Ho et al. (1997)*

The structure of the two jets in the radio regime is seen in Fig. 4.2. The core component of the eastern jet is identified with component A and that of the western jet with component B. Depending on the frequency component A or B dominates. For all frequencies the eastern jet is more continuous whereas the structure of the western jet is better described by single blobs. In addition the western jet is strongly curved, especially at higher frequencies.

There is also seen an emission gap between the two jets for all resolutions, but most prominent for 5 GHz.

The angular resolution of the 43 GHz image is about 0.5 mas.

It is interesting how an image for 86.2 GHz looks like. Is there a gap, what is the resolution and what does the jet structure look like? At the end of this thesis we will have a quick look at the picture obtained from the GMVA observations at 86.2 GHz.

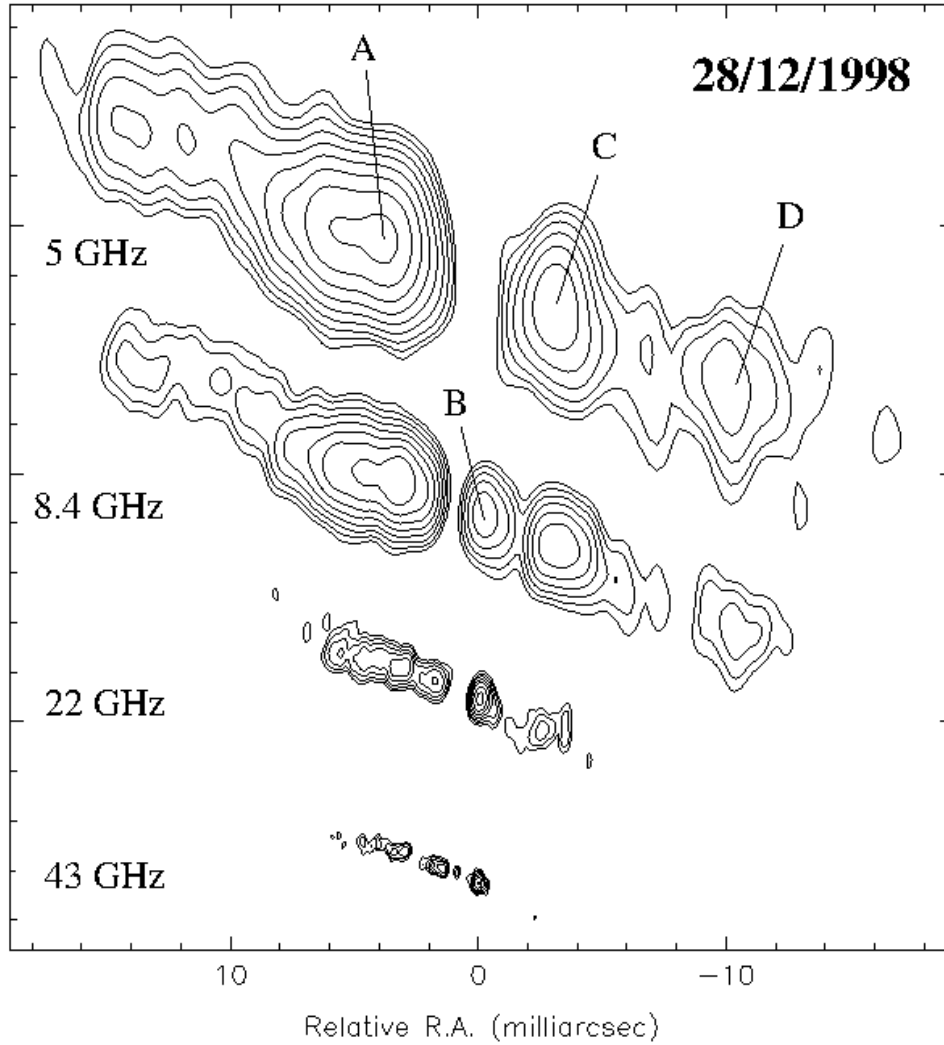


Figure 4.2: *The results of Kadler (2002) show the radio structure of NGC1052 at different wavelengths in 1998*

4.2.2 The GMVA observation

During the observations (observation code GK027) the telescopes observed the calibration source 0235+164 for about one minute, then pointed to NGC1052 for about 3.5 minutes, and then started all over again. This sequence was repeated every 20 minutes from 10 pm at 2004 October 9 to 1:06 pm at 2004 October 10. For that time range there were receiver and pointing problems at Onsala, so there are no data from this telescope. The source was observed by Effelsberg, Pico Veleta, Plateau de Bure, Metsähovi and the VLBA antennas Hancock, Fort Davis, North Liberty, Owens Valley, Pie Town, Kitt Peak, Mauna Kea and Los Alamos. Apart from Hancock, which had receiver problems, the performance of the array was good.

The source of interest was observed for 8 intermediate frequencies (IFs) with 16MHz bandwidth ¹. The DiFX software correlator of the MPIfR in Bonn produced 64 spectral channels for each subband.

In Fig. 4.3 the time coverage of the observation is plotted. Since the source was not always seen by all telescopes due to the curvature of the Earth, there are only a few points where NGC 1052 was simultaneously seen by all instruments..

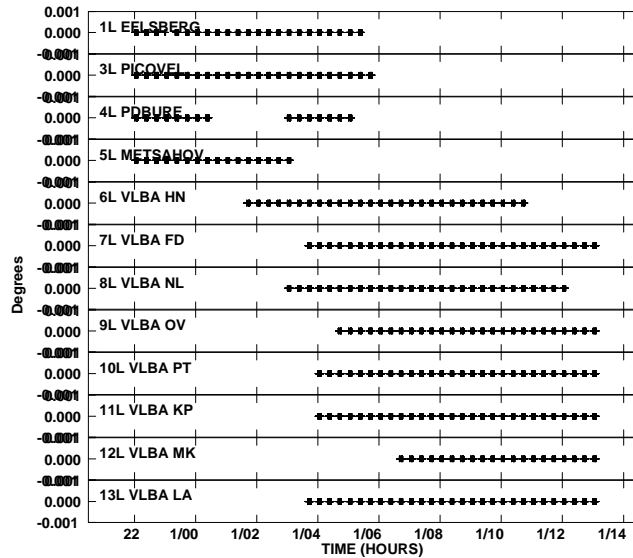


Figure 4.3: Plot to illustrate the time coverage of the observation for each antenna. Plotted is the phase versus the time (in units of observation days), prior to calibration

¹centered at 86.1980, 86.2140, 86.2300, 86.2460, 86.2620, 86.2780, 86.2940 and 86.3100

Looking at the whole observation the uv -coverage can be analyzed, that is a plot of all baselines in the (u, v) -plane. In Fig. 4.4 a very flat structure is seen. That occurs because of the comparatively few very long baselines. Therefore the beam is very elliptical.

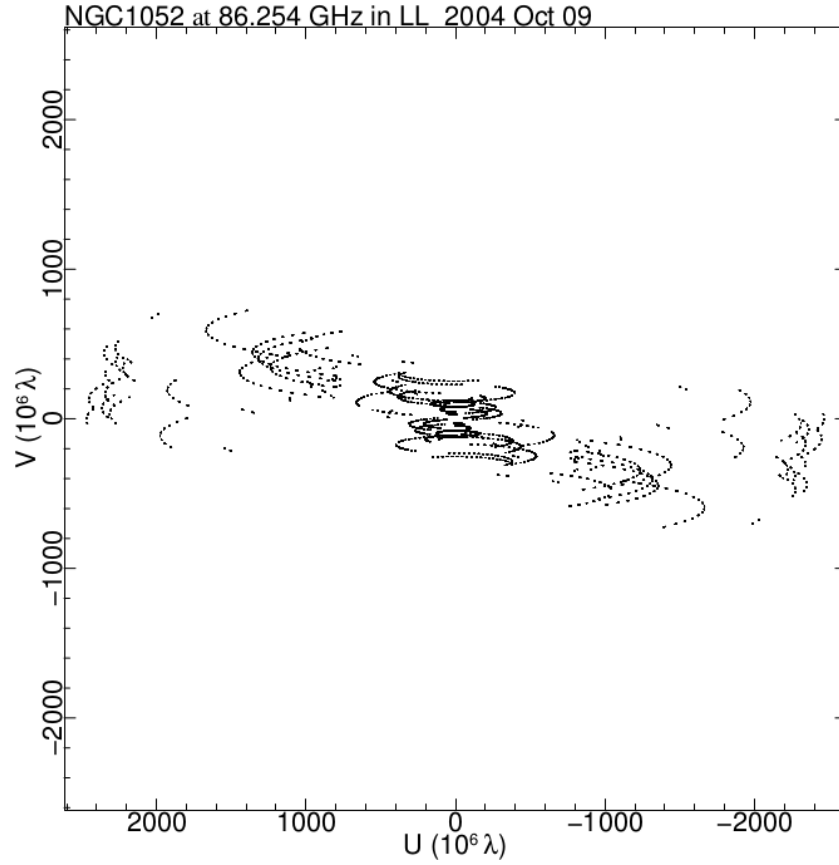


Figure 4.4: uv -plot of the observations of NGC1052 in our experiment. It shows interferometric data from all baselines during the observation (in the (u, v) -plane)

5 | Data Reduction

In Section 3 the “true” visibility was described. True because it is what one would get if everything is perfectly observed and calibrated and there are no errors. It is linked to the brightness distribution via a Fourier transform. But the measured visibility needs to be transformed through calibration processes before you get the true one. The calibration of the data of NGC1052 was the main goal of my Bachelor thesis. This process is usually performed using NRAO’s AIPS software. The necessary steps are discussed in this section.

5.1 Introduction to AIPS

The Astronomical Image Processing System (AIPS) is a program for calibrating VLBI Data. AIPS uses 3 kinds of commands: tasks, verbs and adverbs. Tasks are programs, that can load a file from or to the tape or disc, modify the data or apply changes. Every parameter that can be set is saved via adverbs. Tasks are loaded with “TASK ‘task’” and executed with the verb “GO”. As distinct from this, verbs are at instant executable.

The data to be analyzed are read into AIPS in the FITS-format¹. All informations, like visibilities, antenna coordinates or observation times are read into extension tables to a catalog entry. By selecting the catalog with GETN ‘nn’, where ‘nn’ is the catalog number, and typing “IMH” one gets a first overview of the data. The output looks like the following:

```
AIPS 1: Image=MULTI      (UV)      Filename=GK027      .VLBGLU.    1
AIPS 1: Telescope=VLBI      Receiver=MKIV
AIPS 1: Observer=Bonn Cor      User #= 12
AIPS 1: Observ. date=09-OCT-2004      Map date=15-AUG-2012
AIPS 1: # visibilities 299269      Sort order TB
AIPS 1: Rand axes: UU-L-SIN VV-L-SIN WW-L-SIN TIME1 BASELINE
AIPS 1:          SOURCE  FREQSEL  INTTIM
AIPS 1: -----
AIPS 1: Type      Pixels      Coord value      at Pixel      Coord incr      Rotat
AIPS 1: COMPLEX      3      1.0000000E+00      1.00      1.0000000E+00      0.00
AIPS 1: FREQ      64      8.6197990E+10      33.00      2.5000000E+05      0.00
AIPS 1: STOKES      1      -2.0000000E+00      1.00      -1.0000000E+00      0.00
AIPS 1: IF      8      1.0000000E+00      1.00      1.0000000E+00      0.00
AIPS 1: RA      1      00 00 00.000      1.00      3600.000      0.00
AIPS 1: DEC      1      00 00 00.000      1.00      3600.000      0.00
AIPS 1: -----
AIPS 1: Coordinate equinox 2000.00
AIPS 1: Maximum version number of extension files of type HI is 1
AIPS 1: Maximum version number of extension files of type FQ is 1
AIPS 1: Maximum version number of extension files of type BS is 1
```

¹Flexible Image Transport System: most common astronomical data format

```
AIPS 1: Maximum version number of extension files of type AN is 1
AIPS 1: Maximum version number of extension files of type NX is 1
AIPS 1: Maximum version number of extension files of type CL is 1
AIPS 1: Maximum version number of extension files of type SU is 1
```

Especially the produced tables are interesting, since these access, describe and calibrate the data. In them additional informations attached to the interferometric data are saved. Here is a short explanation of the initial ones:

HI The History table. Here most input and output values of tasks are saved

FQ Information about the IFs ²

BS Solutions for baseline delays, phases and rates, for baseline-based phase calibration

AN Antennas: names and coordinates

NX Information about every observation or scan

CL Calibration table

SU Source specific information

Another task for the initial examining of the data is **LISTR**, with **OPTYPE** “SCAN”, which prints the content of the **NX** table, as well as the observed sources and IFs. For the following calibration this file is needed to search for time ranges in which the calibration source has been observed.

There is a “golden rule”, that is: “data are sanctuary”. So the raw data are never modified. Every calibration step is saved in a table, for example in a solution table (**SN**). Then these values are applied to the original data and the final values including all previous calibration steps are saved in a new calibration table (**CL**).

Very useful is the task **PRTAB**, with that the content of any table can be printed onto the terminal. However, sometimes a plot is more useful. One can examine the time coverage of observations by using **SNPLT**, which plots contents like phase, delay or rate of a **CL** or **SN** table versus the time. (Fig. 5.4, 5.3).

5.1.1 The Most Important Tasks

Before I describe the steps to calibrate the data I will introduce some of the most important tasks and verbs.

FITLD Load the fits file

LISTR Print uv-data and calibration tables. With the help of **LISTR** you can analyze your data very well for the first time.

PRTAB Print the content of a table

SNPLT Plot **CL**, **SN**, **TY** and **PC** tables

LWPLA Pass the defined plot tables to a postscript file

PRTAN Print an antenna file

CLCOR Make corrections to **CL** tables, like adding/removing parallactic angle corrections

POSSM Plot the spectrum (by averaging a dataset): One can plot phase and/or amplitude versus rate

²Intermediate Frequencies

FRING Determine the phase rate calibration. This is the task for the manual fringe fit. The determined delays are saved in a SN table attached to the input file

CLCAL Apply the calibration saved in an SN table to a specified CL table and save it to another CL table

SPLIT Split the data for the different sources

FITTP Save one catalog data to the disk, including the extension tables

5.1.2 The Most Important Vverbs

HELP ‘nn’ Print the help section of the task, verb or adverb ‘nn’

APROPOS ‘nn’ Print everything that has the string ‘nn’ in its name or description

GO Execute a task

TVINI Delete the contents of the TV device, so that one plot is not plotted over the previous one.

UC Print all saved catalogs in this session to the terminal

GETN (nn) Set the values of catalog nn as the input parameters for the actual used task or verb

EXTDEST Delete a table, specified through the adverb inext.

ZAP Delete the catalog, selected by the verb GETN(nn)

5.2 Walk Through The Calibration

The calibration was based on the procedure described by Martí-Vidal et al. (2012). Measured is the Visibility function which has a phase and an amplitude. These are the two quantities that have to be calibrated. Before this is done the positions of the source as well as the telescopes should be correct. To be sure that this is the case, the parallactic angle³ is corrected via the task “CLCOR”, with the adverb OPCODE set to “PANG”. From this task one gets a new CL table. This is the starting point for the next corrections.

For the phase, the first obvious source of errors is the geometrical time delay. But if the positions are correctly determined, these are easy to get. The errors introduced by the single antennas are a more difficult problem. In the last step the amplitudes were corrected for the opacity. An overview is seen in Fig. 5.1

5.2.1 Phase Calibration

The antennas used in the GMVA cover an area from Hawaii over the north American continent up to Finland. So the signal arrives at different times. There is an additional delay, instrumental or not modeled by the correlator between the individual IFs, the subbands. Reasons for this are the difference in the instrumental signal paths as well as other antenna related problems.

But if one wants to profit from the many baselines one needs to correlate the signals. This is only possible if the signals are coherent in time, for the duration of the integration time in the correlator. In addition, one wants to get the “real” signal. If there are too many introduced phases, it is difficult to get back the needed information. So it is indispensable to correct for these delays.

For each baseline one has the phase and amplitude of the Visibility. The phases only depend on the

³the spherical angle between hour circle of the observed object and the great circle, that goes through the Zenith

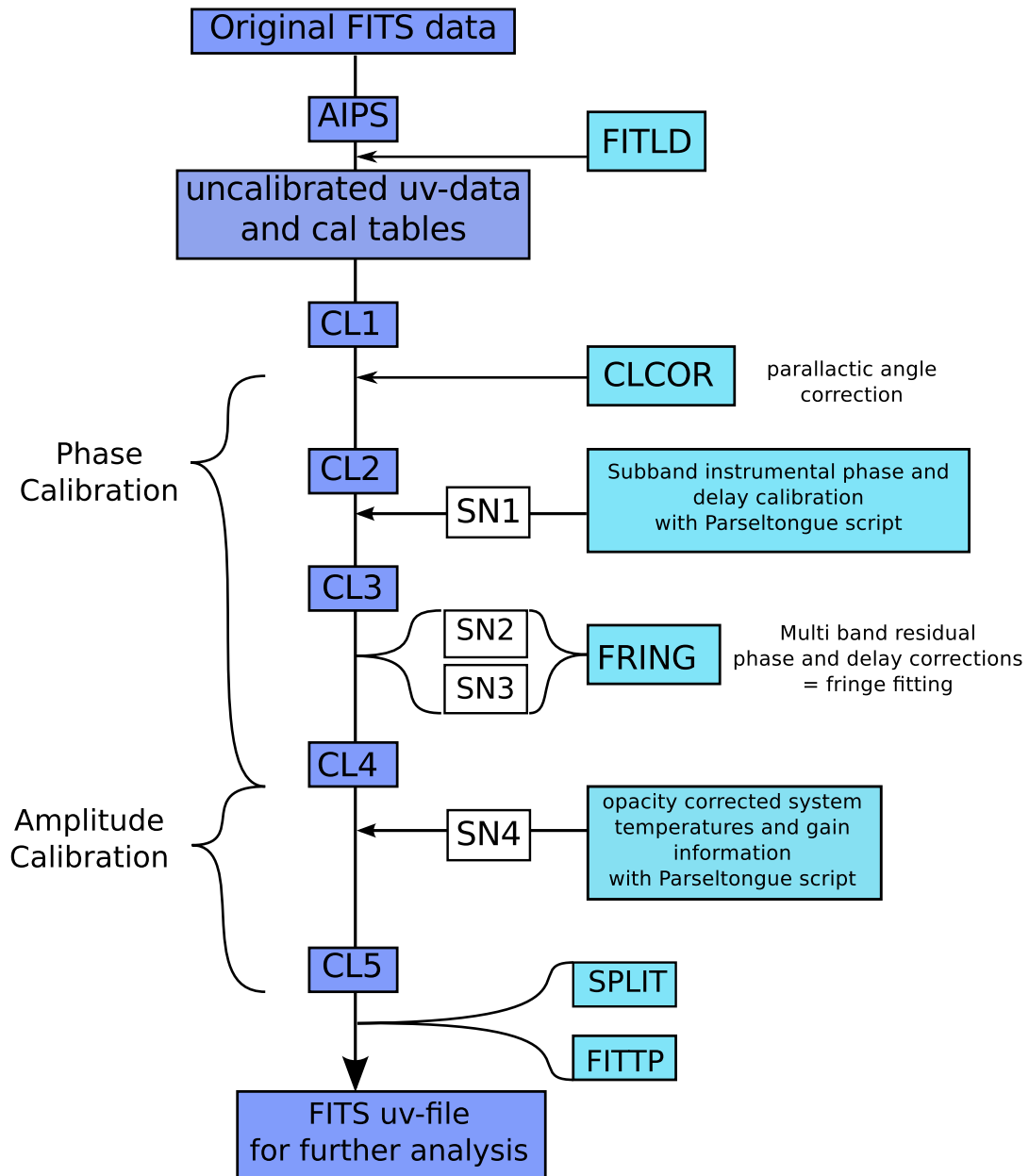


Figure 5.1: the calibration path in AIPS

delays. If the delays are not the same for different IF the phases are “jumping”. This is expected because there are unknown differences caused by the electronics.

The Phase calibration is done in two major steps. First the corrections are found for each IF, the sub-band calibration, so that the phase is basically the same in each one. Only then it is possible to find combined solutions for all IFs of one antenna, the multi-band calibration.

In cm-VLBI the sub-band correction is done by using so called *phase-cal injection tones*. These are inserted in the signal paths and so the phases can be calibrated by searching these pulses. But unfortunately this is not possible for 86 GHz observations, because for this frequency range the receivers of the VLBA do not have these tones. The method I applied is the *manual phase-calibration*.

The phases and rates are found for each sub-band and antenna by means of a strong calibration source. These can be applied to every source and for all times. This is because one can assume that the errors are the same for one antenna and one specific sub band, independent of the source. The whole phase calibration is done with respect to a reference antenna.

The method used here is the “*global fringe fitting*” (GFF), described by Schwab & Cotton (1983). In contrast to the ‘*baseline based fringe fitting*’ it is possible to use data from all baselines simultaneously. This is useful because the already introduced errors are antenna-related and do not depend on a specific baseline. By combining more baselines, the probability of finding fringes is higher. Before concentrating on this method in more detail, let us have a look at the theory of fringes.

The fringe function is the part of the visibility with the phases in it. For example, for two signals that are correlated over a bandwidth $\Delta\nu$ with the center frequency ν_0 the fringe function would be (compare the real part of Eq. 3.3.3) :

$$F(d) = \cos(2\pi i\nu_0\tau_g) \operatorname{sinc}(\pi\mathcal{B}\tau_g). \quad (5.2.1)$$

The sinc function results from the bandpass and the cosine from the correlation of two over the bandwidth uniform signals. It is nice, if it is possible to get the fringe function out of the visibility data. But first the errors have to be subtracted. The more of the fringe function is seen in the phases the more of the errors can be determined. So it is best if there are structures in the plots that gives the fringes. The needed task in AIPS is called “FRING”, that records the calibration values to a SN table.

For the baseline based fringe fitting, the visibility data are first Fourier transformed so that the rate and delay can be derived. It is used, that a maximum in the amplitude leads to the demanded values.

The method of GFF is based on two steps. The main one to obtain the fringe solution is to use the least-square fit to the unknown parameters in the visibility function. For that a model, like a point source, is used. For getting a start position for the fit, another method is used. This is more similar to the baseline based fringe fitting. It is just extended to more baselines by using the ‘closure phase principle’ (see for example Thompson et al. (2001)).

In the following I will present the procedure for the phase calibration. The advantage of FRING is that it can apply a GFF. The goal is finding the fringe phase and rate of change for all baselines to a given reference antenna .

It is a problem that the source is relatively low in declination and so isn’t seen by any telescope at any time. There are only very few measurements where some European and some VLBA antennas detected the source at the same time. The observed source is also so weak, that there can not be seen any fringes at the beginning. Because of that, a calibrator source (0235+164) was observed simultaneously.

If the solutions are good they can also be applied to the real source, which is done in the last step, when using CLCAL to apply the results in the SN table to the CL table. Because of the duration of the observation of about one day and the large distance of the antennas, there are at minimum two reference antennas to be used. It was convenient for the first run of FRING to subdivide the data set in three parts:

- The European baselines
- Common transatlantic baselines
- The VLBA baselines

It is important not to divide the array and so produce sub-arrays. This would decrease the advantages of the size of the array. Transatlantic baselines have to be found, so that there is a connection between Europe and America. In principle I used three reference antennas. The best antenna in the VLBA during the observation was Los Alamos in New Mexico. This telescope is nearly in the center of the VLBA antennas and it has fringes with most of the other VLBA antennas. For Europe the most fringes were found with reference to Pico Veleta in the south of Spain (near Granada). And over the Atlantic Effelsberg in Germany (near Bonn) was a good choice.

The next step is to search for the best possible times for fringing. This was done with the help of POSSM. Fig. 5.2 shows the standard output of this task. Plotted is the amplitude and phase of the visibility against the frequencies in each IFs for one baseline. A time interval for the solution has to be given (adverb solint). The longer this interval is as less uncorrelated errors are included and the better the fringe function is seen. The observational time interval for the calibration source was about one minute, so I set 'solint' to 1. This is the time range in that the data are plotted. In addition, the start- and end-time have to be specified. In the output of LISTR one can see, when the source was observed. But there are a lot of possibilities and it takes a long time until the best range is found.

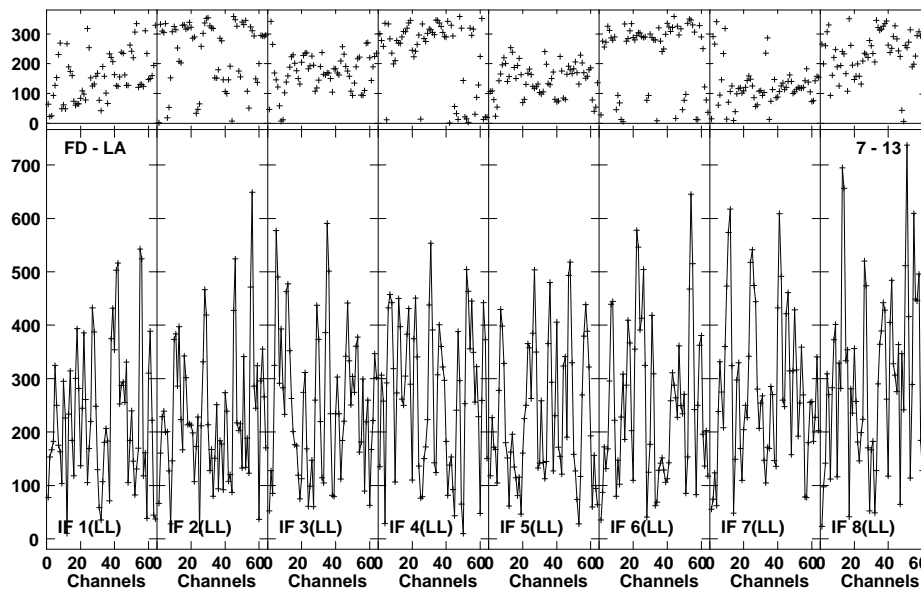


Figure 5.2: POSSM plot of the visibility for the baseline: VLBA LA-KP during 1:07:00 am and 1:08:30 am on Oct. 10, 2004. It is plotted the phase in degrees (upper panel) and the amplitude in units of micro Jansky (lower panel) against the single sub-bands, that are going from 86.1980 GHz to 86.3100 GHz and have a bandwidth of 64 MHz

In the first run of fringe fitting the solutions are searched for each sub band and only for one baseline. It is as consequence not a real GFF, but a manual baseline based phase calibration for only one good baseline. But since FRING works with the GFF it could be that it searches all given antennas if a solution failed. At this step of phase calibration it is possible to calibrate the different antennas at different times but with one reference antenna. So the first corrections are done and the phases of hopefully the most baselines are aligned. For manual calibration one looks in the beginning only for good baselines, so the GFF is a step that is good to perform for the second run of FRING. There one sets the time range to all times and also select all antennas, but lets the task search for fringes for each individual sub band⁴. The best solutions are found by giving FRING a list of antennas to search for fringes. If there are no antennas handed out to the task, it will start to search at the beginning

⁴the used adverb to set is aparm(5) to 0

of the antenna list, if no solution is found with the reference antenna. Most of the times that is not the best possible choice. An additional tool for increasing the sensitivity of FRING is to re-define the automatically by AIPS selected searching windows for rate and delay.

Only if the phases of all baselines are aligned, in the best possible way, there can run an attempt of a multi-band fringe fitting⁵. For all IFs, combined solutions are searched. Now the time range is set to 0 (all times) from the beginning and all antennas are selected. At this stage the main delay was already subtracted and so the delay- and rate-window can be set to a shorter range. When the differences between the single bands are found it is possible to find one solution for all IFs of an antenna.

Everything FRING does is saved in a SN table. For the delay the values are in the range of nanoseconds(see Fig. (5.3)), and for the rate in mHz (see Fig. (5.4)).

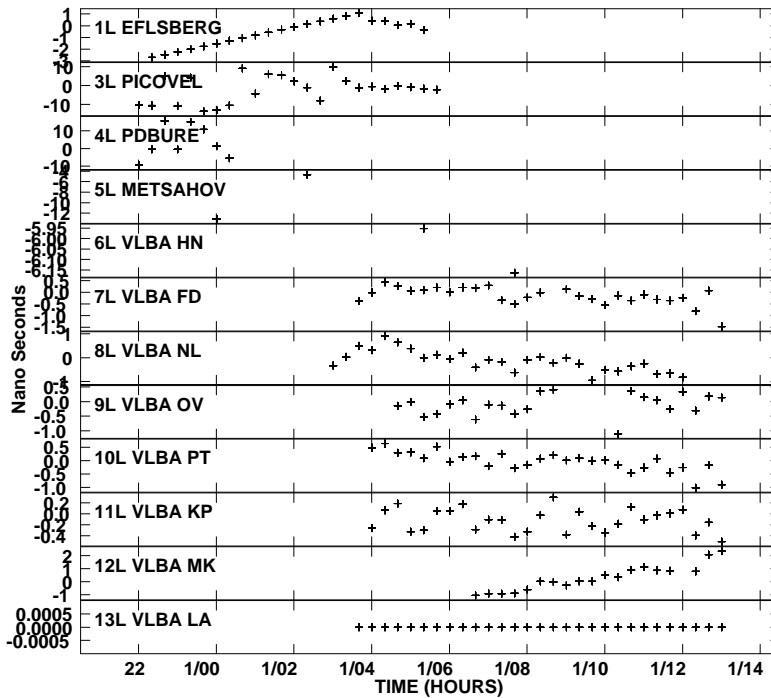


Figure 5.3: *SNPLT plot of the delay at the SN table produced by multi band fringe fitting*

How the phases looks like when applying the changes made by FRING can be visualized by another POSSM plot. For a better overview I have only plotted the phases of the visibility. The amplitudes are corrected separately, so there would not be any differences at this time. In the left column of Fig. 5.5 the phase is plotted against the channels for each IF before calibration. For comparison I plotted the visibility of the baseline LA-Effelsberg, VLBA LA-FD and LA-KP. Since the dish of Effelsberg is greater and hence the sensitivity is larger, the fringes are better to see in baselines with this antenna as in the case of only VLBA antennas.

After all phase calibrations the above mentioned baselines looks like the right hand side panels in Fig. 5.5.

⁵now with aparm(5) set to 1. This means, that combined solutions for all IFs are searched.

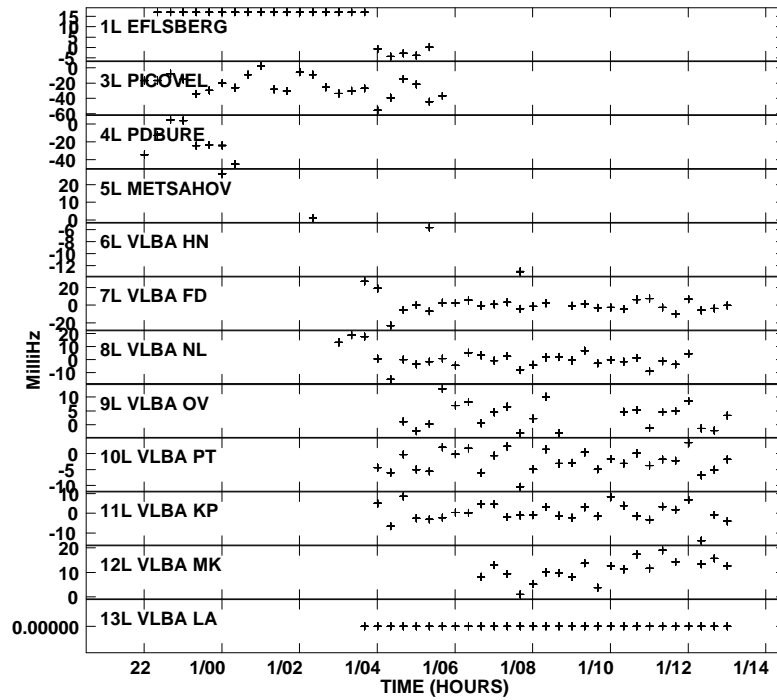


Figure 5.4: *SNPLT* plot of the rate at the *SN* table produced by multi band fringe fitting

Unfortunately the subband phase calibration was not easy to manage manually. A Parsel Tongue script for subband phase calibration as described in Martí-Vidal et al. (2012) could be used. In principle it makes use of the mentioned task *FRING* in finding solutions for each subband. For further analysis only the best values are used. The goal is to align the phases as well as possible to finally find combined solutions for all IFs. This goal is reached by interpolating the found solutions by referring all values in phase and rate to that of one IF. The multi-band fringe fit was done in the way described above.

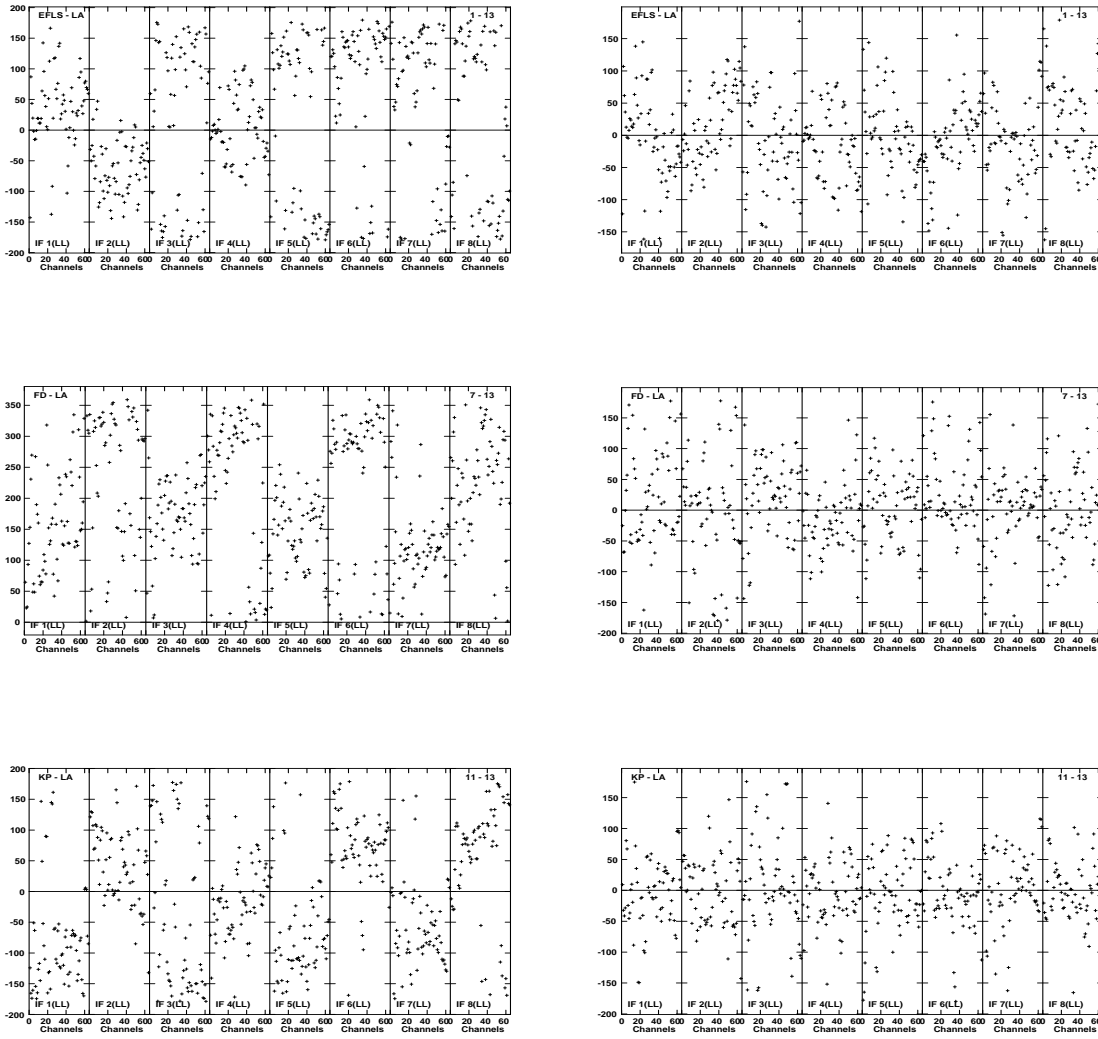


Figure 5.5: *POSSM* plot of the baselines VLBA LA-Effelsberg (between 1:04:40 and 1:04:41), LA-FD (between 1:07:00 and 1:07:01) and LA-KP (between 1:09:20 and 1:09:21). Plotted is the phase against channels of each IF. left: phase before calibration, right: phase after calibration.

5.2.2 Amplitude calibration

The power received at an antenna is in general expressed by an equivalent temperature used in the Planck formula. It describes the power per frequency interval and unit area emitted by a blackbody. A blackbody reflects no light, has a temperature T and emits a characteristic continuous spectrum, known as the blackbody radiation, that is given by:

$$u_\nu d\nu = \frac{2h\nu^3}{c^2} \frac{1}{e^{h\nu/kT} - 1} d\nu \quad (5.2.2)$$

where u_ν is the power per unit area per unit frequency interval and $h = 6.62606876 \times 10^{-34} \text{Js}$ the Planck constant, that gives through $h\nu$ the smallest possible energy quantum of an electromagnetic wave. $k = 1.3806503 \times 10^{-23} \text{JK}^{-1}$ is the Boltzmann's constant, that is known from the theory of

thermodynamics. For small frequencies, thus the Rayleigh-Jeans approximation, this equation can be simplified:

$$u_\nu d\nu = \frac{2kT\nu^2}{c^2} d\nu \quad (5.2.3)$$

The radiation temperature of a resistor at temperature T , expressed through:

$$T_{\text{radiation}} = T \left(\frac{h\nu/kT}{e^{h\nu/kT} - 1} \right) \quad (5.2.4)$$

is used to define the *system temperature* T_{sys} , that specifies the noise power. It is related to the power through $P = kT_{\text{radiation}}\Delta\nu$ (defined by the classical Planck formula), so it is related to a resistor that would produce a power similar to the received. In T_{sys} noise from the receiver as well as from the antenna (unwanted radiation from earth or atmosphere) is included.

The power from the source of interest is expressed in the same manner, as *antenna temperature* T_{ant} , that is related to the flux density.

The last source of noise is the attenuation in the atmosphere. It is described by the *opacity* that is:

$$\tau_{nu} = \int_0^\infty \alpha(\nu, y) dy \quad (5.2.5)$$

(see Thompson et al. (2001)), where α is the power absorption coefficient and y is the distance from the observer.

Normally the atmosphere has only little to no influence in the radio regime. But the observations took place at 86 GHz and there atmospheric absorption has to be taken into account. The noise from the antenna can be neglected, so the only correction to be applied is for the opacity. The opacity τ of the atmosphere is not the same at each station and each time. One gets the opacity through Eq. 5.2.6. That is because the difference between T_{sys} and T_{rec} leaves the attenuation effects and the relation to T_{amb} gives so the opacity.

$$\tau = \log \left(1 - \frac{T_{\text{sys}} - T_{\text{rec}}}{T_{\text{amb}}} \right) \quad (5.2.6)$$

where T_{sys} is the uncorrected system temperature, T_{rec} that of the receiver and T_{amb} is the averaged temperature of the atmosphere.

The amplitude calibration was made with the help of a Parsel Tongue Script following Martí-Vidal et al. (2012). From weather records at each antenna, registered during observation, T_{amb} can be derived. The system temperature is directly measured, sometimes – if using a chopper wheel – already opacity corrected. T_{rec} was estimated “by fitting the lower envelope of the T_{sys} vs. airmass distribution with a linear model. The extrapolation of that model to a null airmass then gives us a reliable estimate of the receiver temperature in the time range considered” (Martí-Vidal et al. (2012), page 6).

As soon as the needed temperatures are estimated and thus the opacity, the system temperature can be corrected through the relation:

$$T_{\text{sys}}^* = T_{\text{sys}} \exp(\tau). \quad (5.2.7)$$

Now these values can be used to calibrate the amplitude of the visibility in AIPS. The corrected system temperatures are loaded into an TY table, with the help of the task “ANTAB”. It produces also a gain curve table (GC). Then the task “APCAL” was used to generate a new SN table, that can be applied as before with “CLCAL”.

6 | Imaging Results

In the previous chapter the calibration strategy was described. Fig. 6.1 shows the amplitude and phase of the interferometric visibilities as a function of frequency for the time range 1:07:00 to 1:07:01 am for the baseline VLBA LA-KP and 1:09:20 to 1:09:21 am for the baseline LA-FD, prior to any phase and amplitude calibration. The final data corrected in phase and amplitude are plotted in Fig. 6.2. The corrections for the phase offsets among the IFs, delay and rates were made for the initial data plotted in Fig. 6.1 (for the phase). The opacity corrections were made for the amplitude.

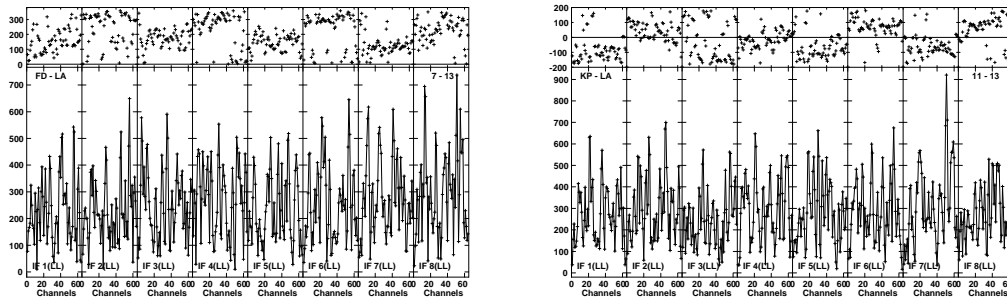


Figure 6.1: POSSM plot of the baselines VLBA LA-KP (time range 1:07:00 - 1:07:01 am) and LA-FD (time range 1:09:20 - 1:09:21 am). Shown are the phase in degrees (upper frame) and amplitude in micro Jansky (lower frame) against channels of each IF in the beginning

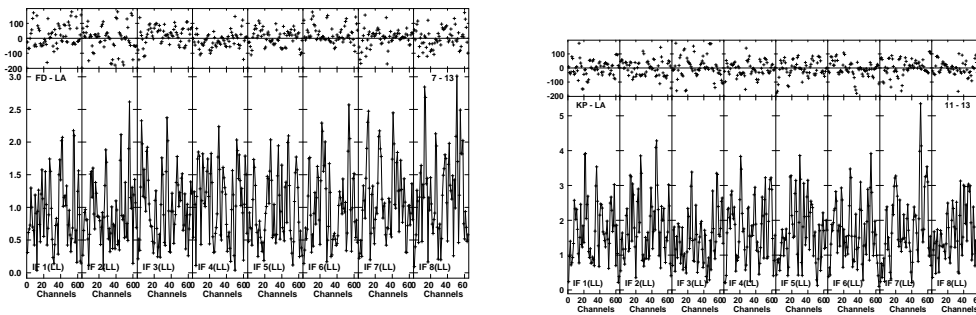


Figure 6.2: POSSM plot of the baselines VLBA LA-KP (time range 1:07:00 - 1:07:01 am) and LA-FD (time range 1:09:20 - 1:09:21 am). Shown are the phase in degrees (upper frame) and amplitude in Jansky (lower frame) against channels of each IF after all the calibrations

During the calibration and especially after the amplitude correction a problem with the data on all baselines involving the Pico Veleta antennas became apparent. The data were not usable and therefore were flagged as bad. We continued the analysis without data from this. The phases rates and delay were computed for Fig. 6.1. The amplitude factor, that converts from correlation coefficient to Jansky, was computed through correction for the system temperature and atmospheric opacity correction.

Even without this important antenna, the data are good enough to proceed with the last steps to get an image. Once the amplitudes and residual phases have been corrected, it is possible to average the data in frequency and time to further analyze them. Our main goal is to obtain an image of the source. To achieve this, we proceed to export the data to AIPS. First we write the multi-source data into a single-source data with the task SPLIT, and then we export the data outside from aips to be analyzed with the DIFMAP software Shepherd et al. (1994). Hybrid mapping with interactive cycles of phase and amplitude self-calibration can be performed, and a final image can be obtained with the help of the CLEAN algorithm Hogbom (1984).

The strategy in DIFMAP is standard and will not be described in more details.

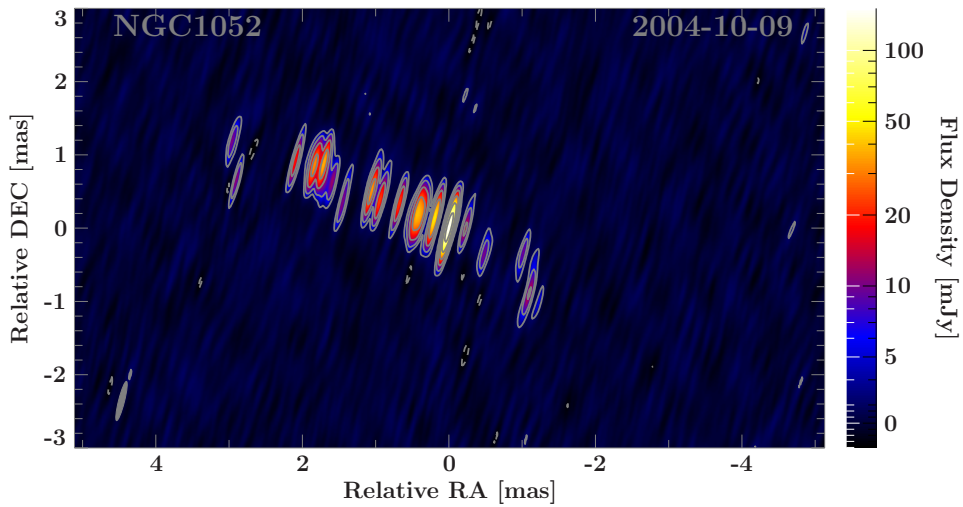


Figure 6.3: Image produced with DIFMAP. The beamsize is 0.551×0.0794 (mas) and the mean peak at 0.149 Jy/beam.

It was a long way until the true visibility was derived and at the end a first-ever image of NGC1052 at an observational frequency of 86.2GHz was created (see Fig. 6.3).

From the image it is not clear, if the component with the most flux is the core of the jet or the counter jet. In comparison Fig. 4.2 shows the radio jet at four smaller frequencies. One can see, that the resolution gets higher when going to 86 GHz. In the area of the jet bases, the structure is much more smaller and so much more exact. The beam of the 86 GHz observation is 0.551×0.0794 mas and so the resolution is about 0.5 mas because of the very elliptical beam.

There are also datasets from 2004 August and 2004 December observed by the MOJAVE survey at 15.4 GHz with a two-jet structure. The data calibrated in this thesis exhibits a look at the inner 3 mas, that are only bad resolved by the MOJAVE image. Since the source is at a distance of 19 Mpc, one mas corresponds to 0.09 pc and we are capable of analyzing the inner 0.3 pc of the jets. Because the beam is only 0.0794 mas in the direction of the jet outflow, there are much more details seen as in the 43 GHz image of 1998.

Now we have a closer look at the 15.4 GHz data from December and the comparison to the 86 GHz observation. From Fig. 6.4 it can not be said which component in the 86 GHz image corresponds to the jet and the counter jet. For that images of the following epochs are needed. We can not be sure that the zero point is the same for each image, the cores of the jet are probably shifted. Further analysis is needed for a better understanding of the structure, but that would exceed the purpose of this thesis.

However, it is obvious that the resolution at 86 GHz is really good and that it is possible to handle the difficulties in data analysis at this frequency. It is worth to pay attention to this progress in radio astronomy and to even improve the techniques, especially in the area of data calibration.

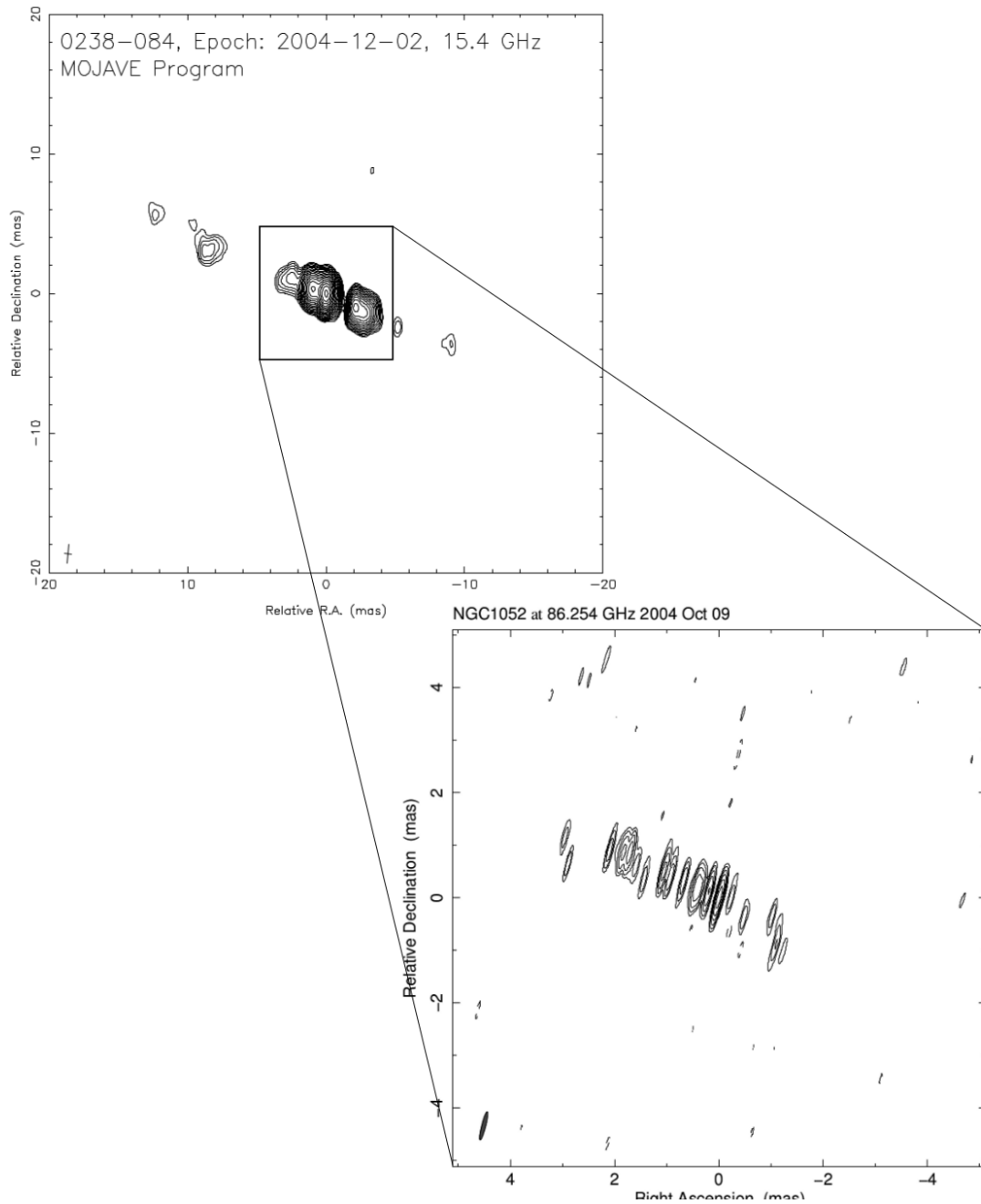


Figure 6.4: Zoom into a 15 GHz MOJAVE image of NGC1052 taken in December 2004. The 86.2 GHz provides a look at the inner 5 mas of the two-sided jet.

Summary

The goal of this thesis was the calibration and imaging of a *mm*-VLBI observations of NGC 1052. The observation took place on 2004, October 9, and 10, with 13 telescopes of the Global mm VLBI Array (GMVA), including Effelsberg, Pico Veleta, Plateau de Bure, Metsähovi in Europe and 8 antennas of the VLBA (in the USA). It was observed using 8 sub-bands with a bandwidth of 16 MHz (centered between 86.1980 GHz and 86.3100 GHz). Between these sub-bands delays occurred, instrumental or not modeled by the correlator.

With the task FRING, the interferometric delay and rate delay were found and the phases were corrected. This task uses the “*global fringe fitting*” algorithm. At a wavelength of 3.6 mm, the atmospheric changes cannot be neglected and therefore the amplitude was corrected for the opacity. This was done by recording the weather data at each station and the measured calibration values as well as the technical characteristics of the observing dishes.

The calibration was a challenging task, but in the end the data were calibrated and read out of AIPS and into DIFMAP. Hybrid mapping was applied to produce the first-ever image of NGC 1052 at 86.2 GHz. NGC 1052 has two radio-emitting jets and the results provide a zoom into the inner 3 mas (corresponding to 0.3 pc). The resolution at this high frequency (with a beam of 0.551×0.0794 mas) is considerably better than previous observations at 43 GHz.

The results of this thesis show the innermost structure of the jet bases. More observations at 86.2 GHz would allow us to study the time evolution of the inner 0.3 pc of the AGNs jets at the highest observing frequency currently accessible by VLBI.

Bibliography

- Antonucci R., 1993, *Ann. Rev. Astron. Astrophys.* 31, 473
- Antonucci R.R.J., Miller J.S., 1985, *ApJ* 297, 621
- Barth A.J., Filippenko A.V., Moran E.C., 1999, *Astrophys. J., Lett.* 515, L61
- Burke B.F., Graham-Smith F., 2009, *An Introduction to Radio Astronomy*, Cambridge University Press, Cambridge, United Kingdom
- Carroll B.W., Ostlie D.A., 2007, *An introduction to Modern Astrophysics*, 2nd Edition, Pearson Addison Wesley, San Francisco, USA
- Denicoló G., Terlevich R., Terlevich E., et al., 2005, *MNRAS* 356, 1440
- Diamond P.J., 1995, In: Zensus J.A., Diamond P.J., Napier P.J. (eds.) *Very Long Baseline Interferometry and the VLBA*, Vol. 82. Astronomical Society of the Pacific Conference Series, p. 227
- Fanaroff B.L., Riley J.M., 1974, *MNRAS* 167, 31P
- Heeschen D.S., Puschell J.J., 1983, *Astrophys. J., Lett.* 267, L11
- Ho L.C., Filippenko A.V., Sargent W.L.W., 1997, *ApJS* 112, 315
- Hogbom J.A., 1984, In: Roberts J.A. (ed.) *Indirect Imaging. Measurement and Processing for Indirect Imaging.*, p. 247
- Kadler M., 2002, *Master's thesis*, Friedrich-Wilhelms-Universität Bonn
- Knapp G.R., Faber S.M., Gallagher J.S., 1978, *ApJ* 83, 139
- Lawrence A., 1987, *PASP* 99, 309
- Lind K.R., Blandford R.D., 1985, *ApJ* 295, 358
- Lobanov A.P., 1998, *A&AS* 132, 261
- Martí-Vidal I., Krichbaum T.P., Marscher A., et al., 2012, *A&A* 542, A107
- Mayall N.U., 1939, *PASP* 51, 282
- Mukhanov V., 2005, *Physical foundations of Cosmology*, Cambridge University Press, Cambridge
- NRAO 2011, *AIPS Cook Book*, The National Radio Astronomy Observatory
- Perucho M., 2008, *Relativistic Outflows and R(M)HD Numerical Simulations*, Lecture slides of the 3rd estrela Workshop in the MPIfR in Bonn
- Reber G., 1988, *JRASC* 82, 93
- Rees M.J., 1966, *Nature* 211, 468
- Rybicki G., Lightman A., 2004, *Radiative Processes in Astrophysik*, Wiley, New York, USA
- Schwab F.R., Cotton W.D., 1983, *AJ* 88, 688
- Shepherd M.C., Pearson T.J., Taylor G.B., 1994, In: *BAAS*, Vol. 26. Bulletin of the American Astronomical Society, p.987
- Thompson A., Moran J., Sweson J.G., 2001, *Interferometry and Synthesis in Radio Astronomy*, 2nd Edition, Wiley, New York, USA
- Urry C.M., Padovani P., 1995, *PASP* 107, 803
- Walker R.C., 1999, In: Taylor G.B., Carilli C.L., Perley R.A. (eds.) *Synthesis Imaging in Radio Astronomy II*, Vol. 180. Astronomical Society of the Pacific Conference Series, p. 433
- Wilms J., Kadler M., 2010, *Galaxies and Cosmology*, Lecture slides WS 2010/2011 University Erlangen-Nürnberg
- Wrobel J.M., 1984, *ApJ* 284, 531

Danksagung

Ich möchte mich ganz herzlich für die viele Unterstützung bedanken, die mir sowohl im Kreise der Re-meiser als auch in Würzburg zu Teil wurde. Ohne die vielen anregenden Gespräche zu astronomischen Themen und die familiäre Atmosphäre hätte ich meine Begeisterung für die Astronomie vielleicht nicht bis zum heutigen Tage behalten.

Ganz besonders möchte ich meinen beiden Betreuern, Matthias Kadler und Jörn Wilms danken. Trotz manch organisatorischer Herausforderung haben sie es mir möglich gemacht, meine Bachelorarbeit in dem Gebiet der Radioastronomie zu schreiben. So konnte ich mein bereits aus Tätigkeiten als studentische Hilfskraft an der Sternwarte bestehendes Wissen festigen und erweitern. Dem unerschütterlichen Enthusiasmus von Matthias Kadler habe ich es zu verdanken, weder den Mut noch den Spaß verloren zu haben.

Ohne die tatkräftige Hilfe von Eduardo Ros hätte ich an mancher Stelle nicht mehr weiter gewusst. Er hatte immer ein offenes Ohr für meine Probleme und einen guten Rat, der mich vorwärts gebracht hat. Durch seine Erfahrung war es mir möglich die Technik der VLBI-Kalibration sowie die vielen damit verbundenen Probleme besser zu verstehen. Vielen Dank dafür!

I would like to thank Ivan Martí-Vidal especially for his help with the AIPS task FRING and the amplitude calibration. His Parseltongue scripts helped to increase the quality of the calibration. He also helped me to understand the routines of fringe fitting.

Es ist angenehm und auch hilfreich sich an Menschen wenden zu können, die ebenfalls noch studieren oder mit ihrer Promotion beschäftigt sind. Während der ganzen Bachelorarbeits-Phase konnte ich immer auf Gespräche mit Robert zählen, wodurch viele der auftretende Probleme gelöst werden konnten. Besonders hervorheben möchte ich noch Christoph und Nela, die mir stets bei allen programmiertechnischen und theoretischen Fragen weiter halfen und sich gerne auf Diskussionen mit mir einließen.

Zu allerletzt wäre ich wahrscheinlich gar nicht hier und würde Physik studieren, wenn mir Familie und Freunde nicht so den Rücken stärken würden. Ein großer Dank geht an meinen Vater, der mir sowohl durch seine Unterstützung als auch durch sein Interesse an meinem Studienfach das alles erst möglich gemacht hat. Die zum Teil sehr lang andauernden physikalischen Diskussionen mit Hannes haben mich fortwährend darin bestärkt, dass ich mit meinem Studium die richtige Wahl getroffen habe. Als treuen Mensa und Tee-Pausen Begleiter möchte ich Sebastian ganz herzlich danken. Ohne diese Ablenkungen hätte ich das eine oder andere Mahl wohl vergessen.

A | Erklärung

Hiermit erkläre ich, diese Bachelorarbeit in Eigenarbeit angefertigt zu haben, sofern nicht explizit in Text oder Referenzen vermerkt. Diese Arbeit ist der Universität Erlangen-Nürnberg als Voraussetzung für den Erhalt des Abschlusses "Bachelor of Science" vorgelegt worden. Ich erkläre, dass diese Arbeit weder partiell noch als Ganzes für den Erhalt eines anderweitigen Abschlusses verwendet wurde und wird.

Erlangen, den

Anne-Kathrin Baczko